Astrocytes mediate long-lasting synaptic regulation of ventral tegmental area dopamine neurons

Linda Maria Requie [1,9], Marta Gómez-Gonzalo [1,9] ✉, Michele Speggiorin [1,9], Francesca Managò [2], Marcello Melone[3], Mauro Congiu[4,5], Angela Chiavegato[1], Annamaria Lia [1], Micaela Zonta [1], Gabriele Losi[1,8], Vanessa Jorge Henriques[1], Arianna Pugliese[3], Giada Pacinelli[2,6], Giovanni Marsicano[7], Francesco Papaleo [2], Anna Lisa Muntoni[5], Fiorenzo Conti[3] & Giorgio Carmignoto [1]✉

The plasticity of glutamatergic transmission in the ventral tegmental area (VTA) represents a fundamental mechanism in the modulation of dopamine neuron burst firing and phasic dopamine release at target regions. These processes encode basic behavioral responses, including locomotor activity, learning and motivated behaviors. Here we describe a hitherto unidentified mechanism of long-term synaptic plasticity in mouse VTA. We found that the burst firing in individual dopamine neurons induces a long-lasting potentiation of excitatory synapses on adjacent dopamine neurons that crucially depends on Ca^{2+} elevations in astrocytes, mediated by endocannabinoid CB1 and dopamine D2 receptors co-localized at the same astrocytic process, and activation of pre-synaptic metabotropic glutamate receptors. Consistent with these findings, selective in vivo activation of astrocytes increases the burst firing of dopamine neurons in the VTA and induces locomotor hyperactivity. Astrocytes play, therefore, a key role in the modulation of VTA dopamine neuron functional activity.

Dopamine (DA) neurons of the VTA regulate a wide array of physiological functions, including locomotion, attention, motivation and reward-based learning[1–3]. A fundamental step in these DA-dependent functions is the transition of spiking activity in VTA DA neurons from tonic, low-frequency firing at rest to high-frequency bursts that modulate the action of DA by determining the synaptic phasic release of DA at VTA target areas, such as nucleus accumbens (NAc), medial prefrontal cortex, hippocampus and amygdala[4–7]. This transition to bursting activity of DA neurons is under crucial control of glutamatergic afferent inputs to the VTA originating from various brain regions[4,7,8]. Importantly, the enduring changes in the strength of these glutamatergic synapses exert profound effects on DA neurons, regulating their

burst firing mode and DA release at target regions[1,9]. The plasticity of these glutamatergic synapses represents, therefore, a key mechanism in the modulation of DA transmission and DA-dependent behaviors. Although extensive studies highlighted the role of neuronal signals in the synaptic plasticity of VTA circuits[1,10], the role of astrocytes has been insufficiently investigated.

A recent study reported that optogenetic stimulation of channelrhodopsin-expressing VTA astrocytes alters glutamate transport, favoring DA neuron inhibition and avoidance behavior[11]. However, this type of stimulation depolarizes astrocytes, leading to substantial increase in extracellular K^+ and increase in neuronal excitation[12]. Whether astrocytes are functionally recruited to the VTA circuitry by neuronal signals and influence the plasticity of glutamatergic synaptic transmission to VTA DA neurons remains totally unexplored.

Astrocytes are active components of brain circuits. Besides their support and metabolic functions, they respond with Ca^{2+} elevations to neurotransmitters and, in turn, release gliotransmitters that regulate synaptic transmission and plasticity[13–15]. Astrocytes are similarly activated by local signals, such as endocannabinoids (eCBs), released by neurons at somatodendritic levels. In various brain areas, including the VTA, eCBs act as retrograde signals that induce neurotransmitter release depression upon pre-synaptic type-1 cannabinoid receptor (CB1R) activation[16,17]. Studies in hippocampus and dorsal striatum showed that eCBs also target astrocytic CB1Rs, evoking Ca^{2+} elevations and glutamate release that potentiates distant excitatory synapses[18–20]. Whether this lateral potentiation of synaptic transmission is also operative in the VTA is unknown.

Using ex vivo and in vivo approaches, we investigated whether eCBs released by bursting discharges of VTA DA neurons[21] induce a potentiation of glutamatergic transmission to nearby DA neurons and whether this action is mediated by astrocytes. Because VTA DA neurons, beside eCBs, release DA at somatodendritic levels[22], we investigated whether DA is also involved in DA neuron-to-astrocyte signaling. Finally, we evaluated the functional consequences of a specific activation of astrocytes in vivo at the level of both VTA DA neuron firing and locomotor activity. Our results unveil a reciprocal functional signaling between DA neurons and astrocytes in VTA circuits.

Results

Lateral LTP of EPSCs in VTA DA neurons of young female mice

We investigated whether the bursting activity in individual DA neurons evokes lateral potentiation of glutamatergic transmission[18]. In VTA slices of postnatal day (P)14–17 C57BL/6J female mice, we recorded from pairs of neurons showing the typical features of DA neurons (Fig. 1a and Extended Data Fig. 1a–d). In one neuron of the pair, we monitored excitatory post-synaptic currents (EPSCs) evoked by low-frequency stimulation of rostral glutamatergic afferents. To the second neuron, located 70–120 µm apart, through intracellular current pulses we imposed the burst firing mode that characterizes in vivo DA neuron activity (bursts of five action potentials at 20 Hz, 2-Hz inter-burst frequency and 5-minute duration; Extended Data Fig. 1e)[23–25]. After bursting activity, EPSC amplitude from the first DA neuron is significantly increased, and this potentiation is maintained for at least 45 minutes (Fig. 1b,d). We define this novel form of lateral synaptic plasticity as burst-induced long-term potentiation (bLTP). Evaluation of the paired-pulse ratio (PPR) revealed a significant PPR reduction 45 minutes after DA neuron bursts, suggesting a pre-synaptic mechanism in bLTP generation (Fig. 1c). This pre-synaptic locus is confirmed by the relative changes of the coefficient of variation (CV) for EPSCs after DA neuron bursts (Fig. 1c). Notably, the induction of a tonic-like discharge that mimics basal DA neuron activity (2-Hz action potential frequency for 5 minutes; Extended Data Fig. 1e) fails to modify evoked EPSCs in adjacent DA neurons at any timepoint tested (Extended Data Fig. 1f), indicating that bLTP depends on DA neuron bursting activity. Consistently, the PPR is not modified 30 minutes after DA neuron tonic firing (basal

conditions (bsl), 1.045 ± 0.08; 30 minutes after tonic firing, 1.056 ± 0.1; P = 0.827, paired t-test; Extended Data Fig. 1g). The long-lasting potentiation is not observed in age-matched male mice (Fig. 1b,d), in which EPSC amplitude is only transiently increased 3 minutes after bursts (Fig. 1b). We did not further investigate this short-term potentiation, and we focused the present study on the bLTP generation mechanism.

### Generation of bLTP requires astrocytic Ca^{2+} elevations

To understand whether astrocytes are involved in bLTP generation, we performed experiments in P14–17 type-2 inositol 1,4,5-trisphosphate receptor knockout (IP3R2$^{-/-}$) female mice in which G-protein-coupled mediated astrocyte Ca^{2+} elevations are largely impaired[19,26,27]. In contrast to the bLTP observed in wild-type (WT) C57BL/6J mice, in VTA slices from IP3R2$^{-/-}$ female mice, DA neuron bursts evoke only a transient potentiation of synaptic transmission (Fig. 1d). Additional experiments in IP3R2$^{-/-}$ and IP3R2$^{+/+}$ littermates confirm that DA neuron bursts in IP3R2$^{-/-}$ littermates fail to evoke bLTP, whereas IP3R2$^{+/+}$ littermates show a bLTP similar to that of WT mice (Extended Data Fig. 2). Dialysis of the Ca^{2+} chelator BAPTA in the astrocyte syncytium, which blocks Ca^{2+} signaling in astrocytes[28], also prevents bLTP (Fig. 1d). These data suggest that bLTP induction depends on IP3R2-mediated astrocytic Ca^{2+} elevations induced by signals generated by DA neurons. This hypothesis was directly tested in VTA slices from WT and IP3R2$^{-/-}$ mice loaded with the Ca^{2+} fluorescent indicator Fluo-4 and the specific astrocytic marker SR101. To monitor Ca^{2+} signals from astrocytes in proximity of soma and dendrites, through a patch pipette we filled DA neurons with the fluorescence tracer neurobiotin (Fig. 1e). We observed that DA neuron bursts evoke in astrocytes of female, but not male, mice Ca^{2+} elevations that last for at least 25 minutes (Fig. 1f–h). Furthermore, DA neuron bursts fail to evoke astrocyte Ca^{2+} elevations in IP3R2$^{-/-}$ female mice and also in WT female mice after loading the astrocyte syncytium with BAPTA (Fig. 1h and Extended Data Fig. 2c). Overall, these data suggest that astrocyte IP3R2-mediated Ca^{2+} elevations are required for bLTP generation.

Generation of bLTP requires eCB, DA and mGluR1 signaling

To gain further insights into the molecular mechanism of bLTP generation, we investigated whether CB1 and/or DA receptors (Rs), activated by eCBs and/or DA locally released by VTA DA neurons, are involved. We found that applications of either the CB1R antagonist AM251 or the D2-type receptor antagonist eticlopride prevent bLTP, whereas the D1R antagonist SCH-23390 hydrochloride is ineffective (Fig. 2a; compared to controls, AM251 P = 0.046, eticlopride P = 0.045 and SCH-23390 P = 0.916, Mann–Whitney rank-sum test). We also evaluated the role of the N-methyl-D-aspartate receptor (NMDAR), which mediates synaptic plasticity in different brain regions[29], including the VTA[10]. We found that bLTP is unaffected by the NMDAR antagonist D-AP5 (Fig. 2a; compared to controls, P = 0.584, unpaired t-test), suggesting that NMDAR is not involved. We then observed that bLTP is abolished by the type-1 metabotropic glutamate receptor (mGluR1) antagonist LY-367385 (Fig. 2a; compared to controls, P = 0.015, unpaired t-test), indicating that, as previously reported in hippocampal[18,19] and striatal circuitries[20], the astrocyte action is mediated by mGluR1 receptor activation.

We then asked whether CB1 and D2R activation, which is required for bLTP generation, is also required for DA neuron burst-induced astrocytic Ca^{2+} elevations. We found that the astrocyte response is abolished in the presence of either AM251 or eticlopride (Fig. 2b; compared to controls, AM251 P = 0.026, unpaired t-test; eticlopride P = 0.002, Mann–Whitney rank-sum test). In contrast, the astrocyte Ca^{2+} response is unaffected in the presence of the mGluR1 antagonist LY-367385 (Fig. 2b; compared to controls, P = 0.778, unpaired t-test), suggesting that mGluR1 activation plays its crucial role in bLTP generation downstream astrocytic Ca^{2+} signals.

In support of the role of astrocytic CB1 and D2Rs in bLTP, pre-embedding electron microscopy (EM) experiments showed that, besides neurons (Extended Data Fig. 3a and Supplementary Table 1),
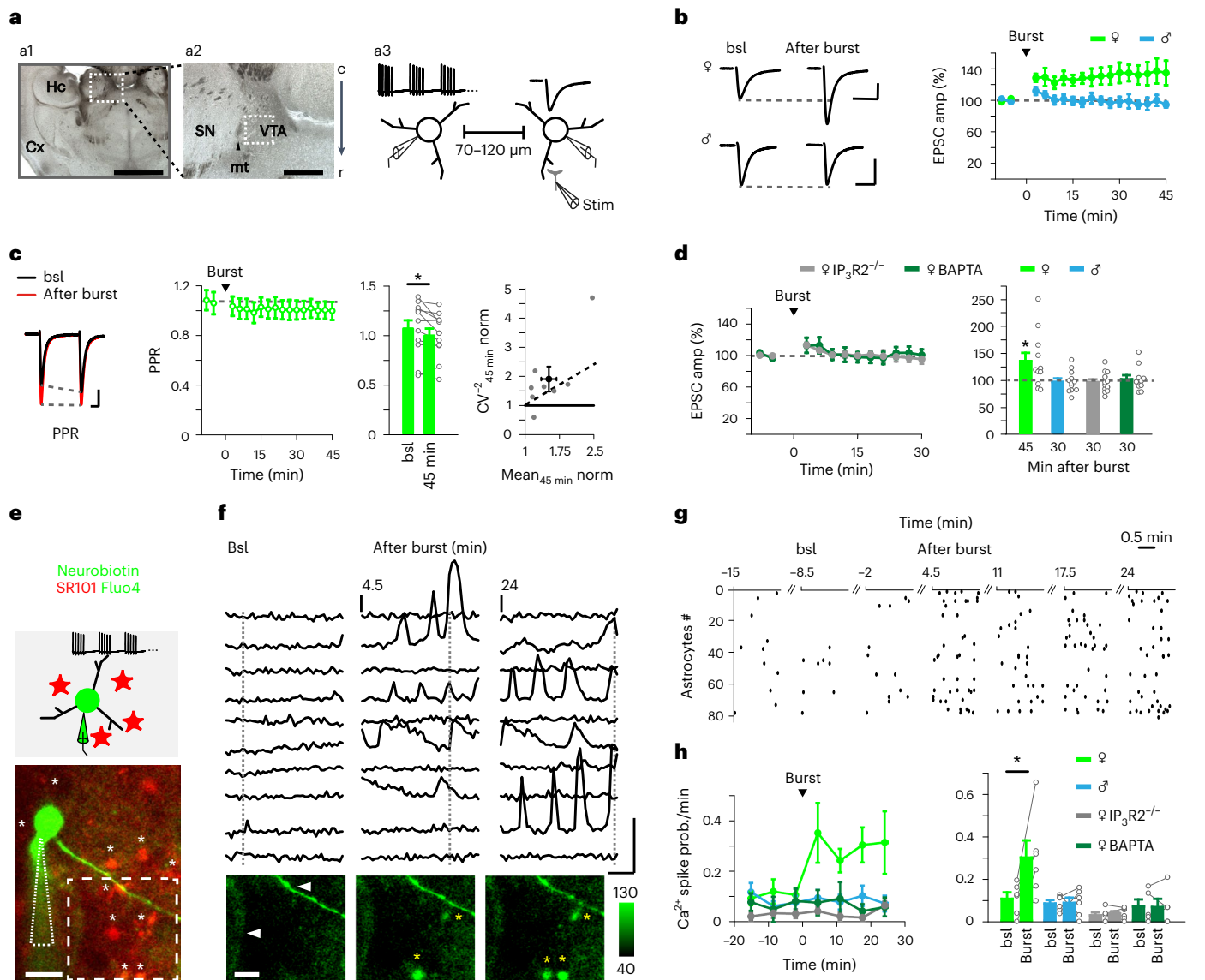
Fig. 1 | Astrocyte recruitment by DA neuron burst firing induces LTP of excitatory synapses onto adjacent DA neurons in young female mice.
a, a1, low magnification from a horizontal brain slice with a caudal-rostral orientation. Cx, cortex; Hc, hippocampus. Scale bar, 1 mm. a2, high magnification of the area indicated in a1. mt, medial terminal nucleus of the accessory optical tract; SN, substantia nigra (lateral to mt); VTA (medial to mt); c, caudal; r, rostral. Dashed square: lateral part of the VTA where DA neuron pair recordings were performed. Scale bar, 200 μm. a3, schematic of the experimental design showing a DA neuron pair, two recording pipettes, the burst firing imposed to a DA neuron (left) and the EPSC evoked on the other DA neuron (right) by stimulation of rostral glutamatergic afferents (Stim). **b**, Left: evoked EPSCs at bsl and 45 minutes after bursts from female (♀) and male (♂) mice. Stimulus artifacts were removed. Scale bars, 50 pA, 20 ms. Right: EPSC amplitude in female ($n = 11$) and male (up to 30 minutes, $n = 12$; up to 45 minutes, $n = 6$) mice after burst firing protocol (arrowhead). In this and the other figures reporting EPSC amplitude versus time, $t = 0$ indicates the end of burst firing. **c**, Left: representative EPSCs (time interval, 50 ms) from a DA neuron of a female mouse, before bursts (bsl, black traces) and after bursts (red traces). Scale bars, 20 pA, 10 ms. Middle: time course of PPR values in female mice ($n = 11$), before and after burst firing protocol (arrowhead). Right: mean PPR values before and 45 minutes after burst firing ($P = 0.037$, two-tailed paired t-test) and analysis of the CV of EPSCs, 45 minutes after burst firing for potentiated cells (black circle, mean value). **d**, Left: EPSC amplitude after burst firing protocol in IP$_3$R2$^{-/-}$ female mice and in WT female mice after

BAPTA (50 mM) dialysis in astrocytes. Right: EPSC amplitude at timepoints indicated after burst firing in different groups (female mice, $n = 11$ from ten mice, $P = 0.044$; male mice, n = 12 from nine mice, $P = 0.664$; IP$_3$R2$^{-/-}$ female mice, n = 12 from ten mice, $P = 0.505$; BAPTA, n = 10 from eight mice, $P = 0.78$; two-tailed one-sample t-test). **e**, Schematic and fluorescence image of a neurobiotin-488-filled DA neuron and SR101-loaded astrocytes (asterisks). Dotted line, patch pipette. Scale bar, 30 μm. **f**, Upper panel: time course of Ca^{2+} levels from astrocytes shown in **e** at basal conditions, 4.5 minutes and 24 minutes after burst firing. Scale bars, 100%, 20 seconds. Lower panel: Fluo-4 fluorescence images of the dashed square shown in **e**. Arrows, two DA neuron dendrites at different focal planes; yellow asterisks, astrocytes displaying Ca^{2+} transients (upper traces) at the timepoints indicated (dashed lines). Scale bar, 20 μm. **g**, Raster plot reporting Ca^{2+} transient onsets from 84 astrocytes, before and after DA neuron burst firing. In this and the other figures reporting the time course of the astrocytic Ca^{2+} spike probability per minute, $t = 0$ indicates burst firing onset. **h**, Left: time course of astrocytic Ca^{2+} spike probability per minute in female mice ($n = 6$ from six mice), male mice ($n = 6$ from four mice), IP$_3$R2$^{-/-}$ female mice ($n = 6$ from three mice) and female mice after BAPTA dialysis in astrocytes ($n = 5$ from three mice), before and after burst firing. Right: Ca^{2+} spike probability per minute before and after burst firing (female mice, $P = 0.026$; male mice, $P = 0.951$; IP$_3$R2$^{-/-}$ female mice, $P = 0.349$; BAPTA, $P = 0.914$; two-tailed paired t-test). In this and the other figures, data are represented as mean ± s.e.m.; *, <0.05; **, <0.01; ***, <0.001; and ****, <0.0001.
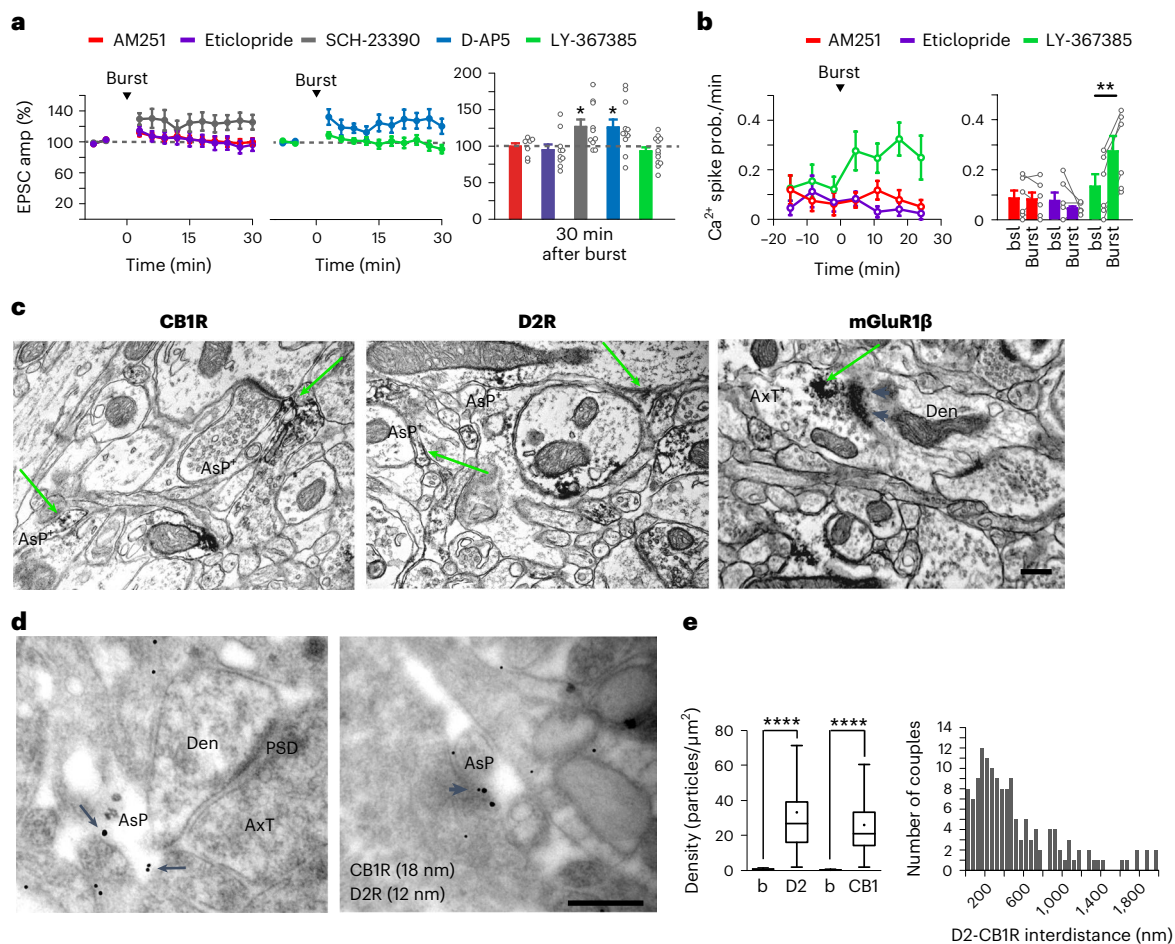
Fig. 2 | Generation of bLTP requires eCB and DA signaling coupled with mGluR1 activation. a, Time course and bar chart of EPSC amplitude in the presence of different antagonists (AM251 (CB1R) 2–4 μM, $n = 7$ from four mice, $P = 0.853$; eticlopride (D2-type R) 1 μM, $n = 10$ from eight mice, $P = 0.495$; SCH-23390 (D1-type R) 10 μM, $n = 10$ from eight mice, $P = 0.026$; D-AP5 (NMDAR) 50 μM, $n = 11$ from nine mice, $P = 0.038$; and LY-367385 (mGluR1) 100 μM, $n = 12$ from nine mice, $P = 0.249$). Two-tailed one-sample t-test. **b**, Time course and bar chart of astrocytic Ca^{2+} spike probability per minute in the presence of antagonists that impair bLTP generation (AM251, $n = 6$ from three mice, $P = 0.818$; eticlopride, $n = 6$ from three mice, $P = 0.351$; and LY-367385, $n = 6$ from four mice, $P = 0.003$). Two-tailed paired t-test. **c**, Pre-embedding EM images from lateral VTA of a young female mouse of CB1, D2 and mGluR1β receptors. Green arrows, immunopositive products in AsP (AsP⁺) and AxT (AxT⁺) forming asymmetric synaptic contacts (arrowheads) with a dendrite (Den). Scale bar, 300 nm. **d**, Post-embedding EM images of CB1/D2R immunogold double-labeled astrocytic processes (AsP) in lateral VTA (CB1R, 18-nm gold particles; D2R,

12-nm gold particles). Left panel: a double-labeled AsP expressing CB1 and D2R (arrows) in close apposition to an asymmetric synapse (AxT, axon terminal; Den, dendrite; PSD, post-synaptic density). Right panel: an edge-to-edge separation distance between these receptors ≤ 50 nm (arrowhead). Scale bar, 300 nm. **e**, Left panel: CB1 and D2R immunogold densities at the membrane of astrocytic processes (AsP, $n = 138$ from four P16 females; D2R, 32.76 ± 2.14 (D2), CB1R, 26.04 ± 1.53 (CB1) gold particles per μm²) and at neuronal nuclei (b, background values, $n = 20$; 0.86 ± 0.08 and 0.46 ± 0.05 for 12-nm and 18-nm gold particles, respectively; $P < 0.0001$, two-tailed Mann–Whitney test). Data are presented as a box and whisker plot. Each box is defined by the 25th and 75th percentiles; the central line indicates the median; and the dot indicates the mean value. The whiskers represent the minimum and maximum values in 1.5× interquartile range. Right panel: distribution of edge-to-edge interdistances (bin, 50 nm) between D2 and CB1 immunogold couples. Except for **e**, data are represented as mean ± s.e.m.

astrocytes express CB1 and D2-type receptors (D2, D3 and D4R; Fig. 2c, Extended Data Fig. 3b and Supplementary Tables 1 and 2). According to our post-embedding quantitative EM analysis of CB1/D2R immuno-gold double-labeled astrocytic processes, CB1 and D2Rs co-localize at peri-synaptic processes (Fig. 2d,e; mean distance: 523.57 ± 38.37 nm), indicating that the same astrocyte can sense both eCBs and DA. Notably, we found that the mGluR1β isoform is expressed at axon terminals making asymmetric synaptic contacts (Fig. 2c, Extended Data Fig. 3c and Supplementary Tables 2 and 3), consistent with a pre-synaptic mechanism of bLTP, as suggested by PPR reduction and CV analysis. Notwithstanding our finding that D1-type receptors are not involved in bLTP, interestingly, we found that functional D1Rs are also expressed in VTA astrocytes (Extended Data Fig. 3e–h, Supplementary Tables 4 and 5 and Supplementary Note 1).

D2R, CB1R and mGluR1 expression in female and male young mice

The bLTP is not observed in young male mice, in which VTA astrocytes fail to respond to DA neuron bursts. This lack of astrocyte Ca^{2+} responses may be due to absence or low levels of CB1 and/or D2Rs. Our EM experiments show that astrocytes from male mice express CB1, D2, D3 and D4Rs (Fig. 3a and Extended Data Fig. 3a,d), but the expression of CB1 and D2Rs is higher in astrocytic processes of female mice than of male mice ($P < 0.0001$; Fig. 3a and Supplementary Table 2), whereas that of D3Rs is higher in male mice than in female mice ($P < 0.0001$; Extended Data Fig. 3d and Supplementary Table 2). Furthermore, the percentage of axon terminals expressing mGluR1β in female mice is twice that observed in male mice ($P = 0.008$; Fig. 3a, Extended Data Fig. 3c and Supplementary Table 2). Therefore, the defective astrocyte Ca^{2+} response
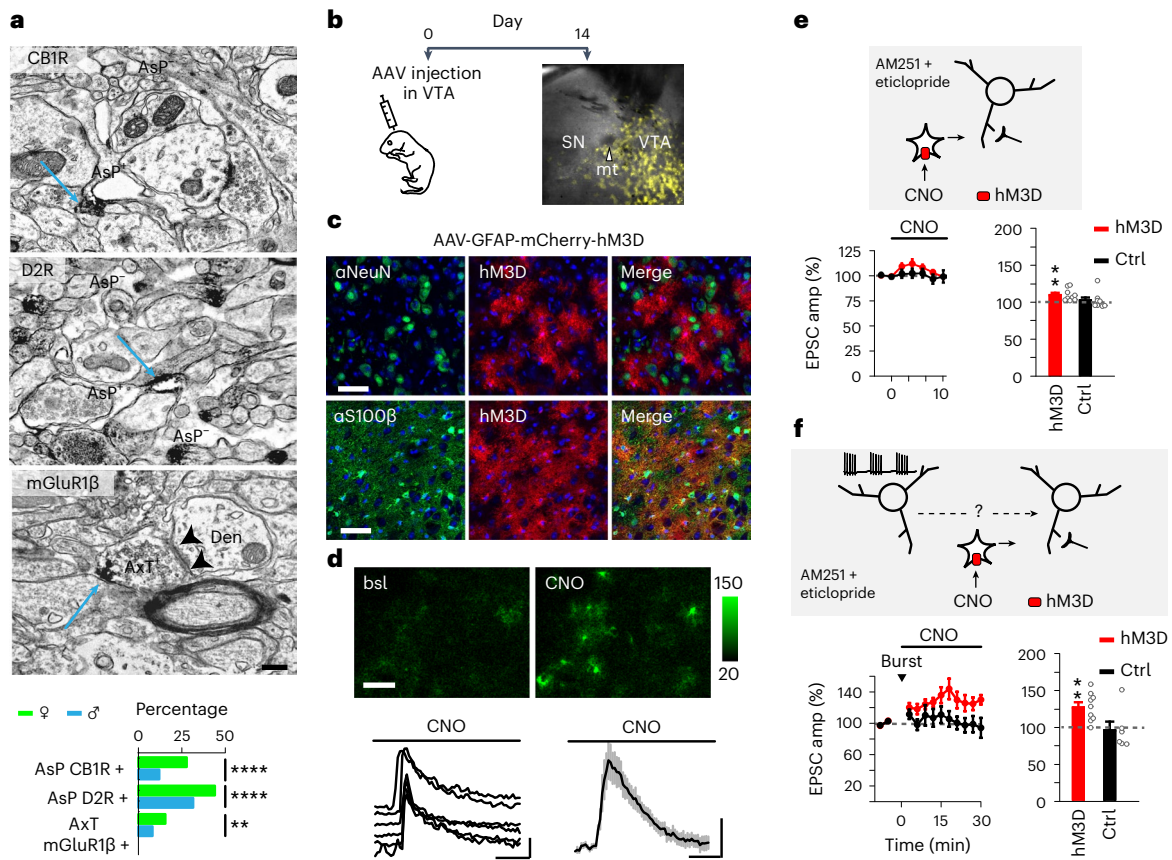
Fig. 3 | Chemogenetic selective activation of astrocytes induces bLTP in young male mice. a, Representative pre-embedding EM images in the lateral VTA from a young male mouse of CB1 and D2R expression at AsP and mGluR1β expression at AxT forming asymmetric synaptic contact (arrowheads) with dendrite (Den). Blue arrows, immunopositive products in AsP (AsP$^+$) and AxT. AsP$^-$, AsP without immunoreactivity. Scale bar, 300 nm. Bottom panel: quantification and comparison (two-sided contingency Fisher's test) of CB1 ($P < 0.0001$, $n = 479$ and 410 total AsP in female and male mice, respectively), D2 ($P < 0.0001$, $n = 554$ and 588 total AsP in female and male mice, respectively) and mGlu1βR ($P = 0.008$, $n = 284$ and 273 total AxT in female and male mice, respectively) expression in female and male mice. **b**, Schematic of the AAV-9/2-hGFAP-hM3D(Gq)_mCherry-WPRE-hGHp(A) injection in the VTA of a neonatal male mouse and fluorescence image of a brain slice 2 weeks after injection (yellow, mCherry-hM3D expression). **c**, Confocal images of the VTA from a mouse injected with AAV-9/2-hGFAP-hM3D(Gq)_mCherry-WPRE-hGHp(A), showing the fluorescence of mCherry-hM3D (red), the nuclear Top-Ro3 (blue) and the specific green fluorescence for either neurons (α-NeuN) or astrocytes (α-S100β). Scale bars, 50 μm. **d**, GCaMP6f fluorescence images of astrocytes at basal conditions and after CNO (10 μM) perfusion. Scale bar, 50 μm. Lower panels: time course of Ca^{2+} elevations evoked by CNO in these astrocytes (left, scale bars, 100%, 30 seconds) and mean change of total Ca^{2+} levels in slices ($n = 9$ from seven mice, mean ± s.e.m.) expressing GCaMP6f and hM3D in astrocytes in response to CNO (right, scale bars, 2%, 30 seconds). **e**, Upper panel: schematic of the experimental design. Lower panel: CNO-induced transient (over the first 9 minutes) increase in EPSC amplitude of DA neurons in male mice expressing hM3D in astrocytes ($n = 9$ from six mice, $P = 0.007$, two-tailed one-sample t-test) but not in non-injected mice ($n = 8$ from five mice, $P = 0.945$, two-tailed one-sample Wilcoxon signed-rank test). **f**, Upper panel: schematic of the experimental design. Lower panel: burst firing coupled with CNO application evokes bLTP (30 minutes) in male mice expressing hM3D in astrocytes ($n = 9$ from eight mice, $P = 0.003$, two-tailed one-sample t-test) but not in non-injected mice ($n = 6$ from five mice, $P = 0.438$, two-tailed one-sample Wilcoxon signed-rank test). Experiments in **e** and **f** were performed in the presence of AM251 and eticlopride. Data are represented as mean ± s.e.m. mt, medial terminal.

to DA neurons in male mice is likely due to reduced CB1R expression and different levels of D2/D3Rs in the astrocytic processes. Whether the low pre-synaptic mGluR1β expression in young male mice contributes to the lack of bLTP is also a plausible hypothesis.

Induction of bLTP in young male mice by astrocyte activation

If the absence of bLTP in young male mice is due, at least in part, to a lack of astrocyte Ca^{2+} responses to DA neuron bursts, we expect bLTP to be observed after coupling DA neuron bursts with astrocyte Ca^{2+} elevations. As a specific astrocyte stimulus, we used chemogenetic activation of Gq-protein-coupled designer receptor exclusively activated by designer drugs (DREADDs, hM3D(Gq)) selectively expressed in astrocytes (Fig. 3b,c and Extended Data Fig. 4). We found that bath perfusion with the hM3D(Gq) agonist clozapine N-oxide (CNO) evokes transient Ca^{2+} elevations in astrocytes expressing hM3D(Gq) and the genetically encoded Ca^{2+} indicator GCaMP6f (Fig. 3d). In agreement

with this transient astrocyte response, parallel experiments performed in the presence of CB1 and D2R antagonists, AM251 and eticlopride, revealed that CNO evokes in male mice expressing hM3Dq in astrocytes, but not in non-injected controls, a short-lasting potentiation of excitatory transmission (Fig. 3e), which becomes full bLTP after coupling CNO with DA neuron bursts (Fig. 3f). Burst firing in DA neurons is, therefore, necessary for bLTP generation, and mGluR1β expression level may be sufficient to mediate bLTP in young male mice. Given that these experiments were performed in the presence of CB1 and D2R antagonists, these results further support that bLTP generation depends on astrocytic, and not neuronal, CB1 and D2Rs.

Previous studies reported that nitric oxide (NO) contributes to long-term synaptic plasticity in different brain circuits[19,30]. The release of NO by burst firing DA neurons may also contribute to bLTP. In female mice, we found that burst firing in DA neurons patched with an NO synthase inhibitor (L-NAME)-containing pipette does not evoke bLTP

but only a transient (6-minute), albeit significant, EPSC potentiation that is not observed in the presence of the other antagonists, which block bLTP (Extended Data Fig. 5a,b). Consistent with this observation, after blocking NO synthesis, DA neuron bursts evoke in astrocytes only a transient Ca^{2+} response (Extended Data Fig. 5c,d), suggesting that NO contributes to astrocyte Ca^{2+} signal dynamics, as previously reported[31]. If NO released by DA neurons has a role in bLTP, we expect bLTP to be observed in young male mice by coupling CNO activation of astrocytes with an NO donor (DEA NONOate), without DA neuron burst induction. Obtained results failed to validate this hypothesis (Extended Data Fig. 5e; see also Supplementary Note 2 for comments on these conflicting results). Further experiments are, therefore, necessary to clarify the role of NO in bLTP.

Female and male adult mice show astrocyte-induced bLTP

We next investigated whether astrocyte-mediated bLTP observed in young mice is also present in young adulthood. We found that, in VTA slices from adolescent/adult mice (P30–70; to simplify, hereafter termed adult mice), DA neuron bursts evoke in adjacent DA neurons a bLTP that is maintained for at least 30 minutes after bursts, and, in contrast to data obtained from young mice, it is surprisingly expressed not only in female mice but also in male mice (Fig. 4a). The presence of bLTP in adult male mice could be due to developmentally regulated expression of CB1, D2 and/or mGluR1β receptors. Quantitative analysis of pre-embedded materials from adult male mice shows that the levels of CB1Rs at astrocytic processes and mGluR1β at excitatory terminals are, indeed, higher in adult male mice than in young male mice, whereas D2R levels are similar (Fig. 4b and Supplementary Table 6). In agreement with the presence of bLTP, our results reveal similar mGluR1β, CB1 and D2 receptor levels in female and male adult mice (Fig. 4b, Extended Data Fig. 6a and Supplementary Table 6). Together with data presented in Fig. 3a,f, these results suggest that the absence of bLTP in young male mice (P14–17) is due to the low expression of astrocytic CB1Rs at this developmental stage.

The mechanism of bLTP in adult mice is similar to that in young female mice, because bLTP is abolished by specific D2, CB1 or mGluR1 receptor antagonists (Extended Data Fig. 6b). To further confirm that bLTP depends on astrocytic, and not neuronal, D2 and CB1Rs, we injected the AAV9/2-hGFAP-mCherry_iCre-WPRE-hGHp into the VTA of male mice carrying a 'floxed' version of either the *Drd2* or the *Cnr1* genes, to express the Cre recombinase in VTA astrocytes (Fig. 4c). Immunohistochemical experiments showed that the great majority of mCherry-Cre-immunopositive cells are also GFAP+ and only a very few mCherry-Cre-immunopositive cells are NeuN+ (Fig. 4d and Extended Data Fig. 7a,b). We found that bLTP is abolished when the Cre recombinase is expressed in astrocytes containing the *Drd2* or *Cnr1* floxed gene but not when it is expressed in astrocytes of WT mice (Fig. 4e and Discussion), validating the central role of astrocytic D2 and CB1Rs in bLTP generation. Finally, as in young female mice, after including the NO synthase inhibitor L-NAME in the patch pipette (Extended Data Fig. 6b), DA neuron bursts induce, rather than bLTP, a small, transient potentiation lasting no more than 6 minutes (EPSC amplitude (%) $t_{6min} = 112.7 \pm 4.4$, $P = 0.028$, $n = 7$). Altogether, these data indicate that the astrocyte-mediated bLTP observed in young female mice is also present in adult female and male mice with similar cellular and molecular mechanism.
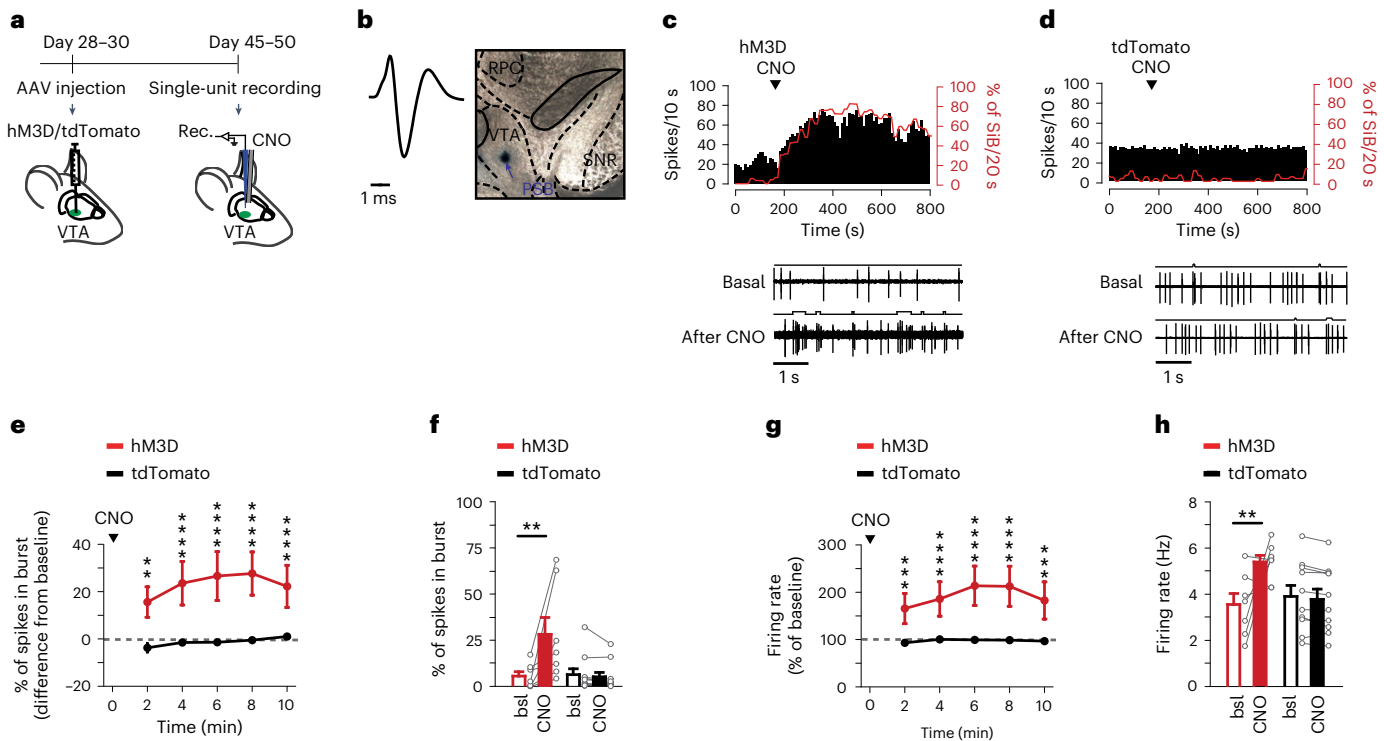
Adult $IP_3R2^{-/-}$ mice show astrocyte Ca^{2+}-dependent bLTP

To further explore the role of astrocyte Ca^{2+} signals in bLTP during adulthood, we performed DA neuron-paired recording experiments from VTA slices of adult $IP_3R2^{-/-}$ female and male mice. Unexpectedly, bLTP was observed (Fig. 4g), although the statistical significance of the potentiation in these mice ($P < 0.05$) is lower with respect to WT mice ($P < 0.01$ and $P < 0.001$, female and male mice, respectively). These results suggest that, in adult $IP_3R2^{-/-}$ mice, the astrocyte Ca^{2+} response to DA neuron bursts is, at least in part, maintained. We, thus, evaluated Ca^{2+} signals in astrocytes of adult male mice that specifically express GCaMP6f (Extended Data Fig. 7c,d). We found that the frequency of spontaneous events at thin astrocytic processes—that is, the so-called microdomains—is lower in $IP_3R2^{-/-}$ mice than in $IP_3R2^{+/+}$ mice (mean event number per minute, $IP_3R2^{+/+}$, 144.6 ± 21.5; $IP_3R2^{-/-}$, 69 ± 16.3; $P < 0.05$, t-test) and tends to be reduced also at the soma (Fig. 4k). However, similarly to $IP_3R2^{+/+}$ mice, in $IP_3R2^{-/-}$ mice DA neuron bursts induce a significant increase in the number of Ca^{2+} microdomains that can account for the presence of bLTP in these mice (Fig. 4h–j). In both $IP_3R2^{+/+}$ and $IP_3R2^{-/-}$ mice, Ca^{2+} response at the soma, mean area and duration of Ca^{2+} microdomains are unchanged after DA neuron bursts, whereas the amplitude is slightly, although significantly, reduced,

Fig. 4 | bLTP is expressed in both female and male, control and $IP_3R2^{-/-}$ adult mice and requires astrocyte Ca^{2+} elevations. a, Presence of bLTP in both female ($n = 15$ from 13 mice, $P = 0.0011$) and male ($n = 14$ from ten mice, $P = 0.0003$) adult mice. Two-tailed one-sample t-test. **b**, Quantification and comparison (two-sided contingency Fisher's test) of CB1, D2 and mGluR1β receptor expression in young and adult male mice ($P < 0.0001$ for CB1, $n = 512$ and 410 AsP in P50 and P16 male mice, respectively; $P = 0.435$ for D2R, $n = 535$ and 588 AsP in P50 and P16 male mice, respectively; $P < 0.0001$ for mGluR1β, $n = 256$ and 273 AxT in P50 and P16 male mice, respectively) and in adult female and male mice ($P = 0.940$ for CB1, $n = 475$ and 512 AsP in P50 female and male mice, respectively; $P = 0.565$ for D2, $n = 691$ and 535 AsP in P50 female and male mice, respectively; $P = 0.346$ for mGluR1β, $n = 262$ and 256 AxT in P50 female and male mice, respectively). **c**, Schematic of the AAV9-hGFAP-mCherry_iCre-WPRE-hGHp(A) injection in adult male mouse VTA and fluorescence image from a brain slice 4 weeks after AAV injection (yellow, mCherry-Cre expression). **d**, Confocal images of the VTA from an adult male mouse injected with AAV9-hGFAP-mCherry_iCre-WPRE-hGHp(A), showing the fluorescence of mCherry-Cre (red), the nuclear Top-Ro3 (blue) and the specific green fluorescence for either neurons (α-NeuN) or astrocytes (α-GFAP). Scale bars, 50 μm. **e**, bLTP is evoked in WT male mice expressing the Cre recombinase in VTA astrocytes ($n = 13$ from ten mice, $P = 0.037$, two-tailed one-sample t-test) and not in *Drd2*-floxed ($n = 9$ from six mice, $P = 0.254$, two-tailed one-sample t-test) or *Cnr1*-floxed ($n = 11$ from eight mice, $P = 0.7$, two-tailed one-sample Wilcoxon signed-rank test) mice. **f**, Confocal images of the VTA from an adult $IP_3R2^{-/-}$ mouse injected with AAV5-GfaABC1D-mCherry-hPMCA2w/b. SV40, showing the expression of the Ca^{2+} pump hPMCA2w/b (α-RFP red staining), the blue nuclear Top-Ro3 and specific green staining for either neurons (α-NeuN) or astrocytes (α-GLT1). Scale bars, 50 μm. **g**, bLTP is evoked in adult $IP_3R2^{-/-}$ mice (female mice, $n = 17$ from 14 mice, $P = 0.035$, two-tailed one-sample Wilcoxon signed-rank test; male mice, $n = 18$ from 16 mice, $P = 0.043$, two-tailed one-sample t-test) but not in $IP_3R2^{-/-}$ mice expressing the Ca^{2+} pump hPMCA2w/b in astrocytes (female mice, $n = 7$ from five mice, $P = 0.475$; male mice, $n = 7$ from five mice, $P = 0.058$; two-tailed one-sample t-test). **h**, Upper panels: left, fluorescence image of an Alexa Fluor 594-filled DA neuron (white dotted line, patch pipette) and tdTomato-expressing VTA astrocytes (red) from an $IP_3R2^{+/+}$ mouse. Scale bar, 10 μm. Right: representative fluorescence images showing Ca^{2+} elevations (arrowheads) from GCaMP6f-expressing astrocytes (scale bar, 2 μm) and corresponding Ca^{2+} signal traces extracted by AQuA (green-marked Ca^{2+} transients, scale bar, 10 seconds, 1 $\Delta F/F_0$). Middle panels: representative image projections and enlarged images of the dashed areas, from 2-minute recordings before (bsl) and after DA neuron bursts, showing Ca^{2+} microdomain events extracted by AQuA (randomly colored). Scale bar, 10 μm. Bottom: raster plots of the microdomain events (black bars) as a function of time, before and after DA neuron bursts. **i**, Same as in **h** but from an $IP_3R2^{-/-}$ mouse. **j**, Time course and statistic evaluation of Ca^{2+} microdomain frequency in astrocytes from $IP_3R2^{+/+}$ mice (6,942 events before burst and 10,760 events after burst in eight slices from six mice, $P = 0.023$, two-tailed paired t-test) and $IP_3R2^{-/-}$ mice (2,483 events before burst and 4,483 events after burst in six slices from four mice, $P = 0.012$, two-tailed paired t-test). **k**, Same as in **j** for somatic events ($IP_3R2^{+/+}$ mice, $n = 26$ astrocytes from eight slices, $P = 0.383$; $IP_3R2^{-/-}$ mice, $n = 16$ astrocytes from six slices, $P = 0.655$; two-tailed paired t-test). Data are represented as mean ± s.e.m. mt, medial terminal.

likely due to the increase in the number of small amplitude events (Fig. 4k and Extended Data Fig. 8). To fully impair Ca^{2+}-dependent astrocytic actions in adult female and male $IP_3R2^{-/-}$ mice, we selectively expressed in astrocytes the plasma membrane Ca^{2+} pump isoform hPMCA2w/b (Fig. 4f and Extended Data Fig. 7e,f) that reduces Ca^{2+} signals in these cells[32]. We found that bLTP generation is fully impaired

in these mice (Fig. 4g). Therefore, also in adult mice, Ca^{2+} signaling is crucial for bLTP generation.

In vivo activation of VTA astrocytes favors DA neuron bursts
Glutamatergic synapses in the VTA circuitry modulate DA neuron firing activity and their potentiation, mainly mediated by NMDARs,

Fig. 5 | Chemogenetic activation of astrocytes in vivo favors burst and overall firing activity in VTA DA neurons. a, Schematic of the experimental design also showing the double pipette for DA neuron recordings (blue) and CNO (1 mM) application (gray). **b**, Left: representative action potential (start to end >2.5 ms) from a putative VTA DA neuron. Right: location of a recorded putative VTA DA neuron. PSB, pontamine sky blue; SNR, substantia nigra pars reticulata; RPC, red nucleus. **c,d**, Upper panels: representative firing rate (spikes per 10 seconds) histograms and percentage of spikes in burst (SiB per 20 seconds) trends over time of VTA DA neurons from mice expressing hM3D (**c**) or tdTomato (**d**) in astrocytes. Lower panel: examples of raw spike traces of the same neurons before and after local CNO applications. **e**, Time course of the bursting activity after local CNO applications (hM3D, *n* = 7 from seven mice; tdTomato, *n* = 10 from five mice). Two-way repeated-measures ANOVA and Bonferroni's multiple comparison test: main effects are not indicated; hM3D 2 minutes versus hM3D

basal **$P < 0.01$; hM3D 4, 6, 8, 10 minutes versus hM3D basal ****$P < 0.0001$. **f**, Percentage of SiB before and after local CNO applications (hM3D, *n* = 7 from seven mice; tdTtomato *n* = 10 from five mice). Two-way repeated-measures ANOVA and Bonferroni's multiple comparison test: main effects are not indicated; hM3D after CNO versus hM3D basal **$P < 0.01$. **g**, Time course of the firing rate after local CNO applications (hM3D, *n* = 7 from five mice; tdTomato, *n* = 10 from seven mice). Two-way repeated-measures ANOVA and Bonferroni's multiple comparison test: main effects are not indicated; hM3D 2, 10 minutes versus hM3D basal ***$P < 0.001$; hM3D 4, 6, 8 minutes versus hM3D basal ****$P < 0.0001$. **h**, Firing rate before and after local CNO applications (hM3D, *n* = 7 from five mice; tdTomato, *n* = 10 from seven mice). Two-way repeated-measures ANOVA and Bonferroni's multiple comparison test: main effects are not indicated; hM3D after CNO versus hM3D basal **$P < 0.01$. Data are represented as mean ± s.e.m.

enhance DA neuron bursts, thus playing a key role in DA-dependent function and dysfunction[1,33]. Because astrocytes, as we show here, also induce a potentiation of these glutamatergic synapses, we asked whether in vivo astrocyte activation increases the burst firing mode of VTA DA neurons and eventually affects behavior. We injected AAV9-GFAP-hM3D(Gq)-mCherry or AAV5.GfaABC1D.cyto-tdTomato. SV40 in the VTA of adult male mice (Fig. 5a), specifically targeting astrocytes (Extended Data Fig. 9). Astrocytes were activated through brief pressure pulses applied to a CNO-containing glass pipette (Methods) while recording the firing activity from individual VTA neurons, showing the typical features of DA neurons (Fig. 5a,b). This approach warrants that only VTA astrocytes in proximity of the recorded neuron are stimulated, ruling out the activation of possible mistargeted astrocytes in regions surrounding the VTA. Consistent with the astrocyte-mediated enhancement of glutamatergic transmission to DA neurons observed in VTA slices, astrocyte activation by CNO increases the bursting discharges of all putative DA neurons that persist for at least 10 minutes (Fig. 5c,e,f), and it also increases the overall firing rate in five of seven DA neurons recorded (Fig. 5g,h). In contrast, DA neuron activity in tdTomato-expressing mice is unaffected by CNO, in terms of percentage of spikes in bursts and firing rate (Fig. 5d–h). These in vivo data show that astrocytes exert a direct control on VTA DA neuron firing activity.

In vivo activation of VTA astrocytes induces hyperlocomotion
The dopaminergic system plays a central role in the control of locomotor activity[3]. We, thus, evaluated whether the selective activation of astrocytes, which increases VTA DA neuron burst firing, controls locomotor activity. Locomotion was tested in male mice given bilateral VTA injections of AAV9-GFAP-hM3D(Gq)-mCherry (hM3D) or AAV8-GFAP-GFP (GFP) (Fig. 6a,b). Thirty minutes after intraperitoneal (i.p.) injections, CNO induces a locomotor hyperactivity in hM3D-injected mice as compared to GFP control mice (Fig. 6c–e). The time spent at the center was similar in the two groups (Fig. 6f), suggesting no major effects on anxiety-like phenotypes. Interestingly, 48 hours after CNO, a significant locomotor hyperactivity was still observed in hM3D mice over the first 10 minutes of the task (Fig. 6c–e). Although we cannot rule out that possible mistargeted astrocytes in the substantia nigra (SN) contribute to the action of astrocytes described above, recent studies reveal that DA neurons of the VTA, and not those of the SN, play a major role in the induction of motor hyperactivity[3,34,35]. Overall, these in vivo data show that activation of astrocytes enhances VTA DA neuron firing activity and induces locomotor hyperactivity.

Discussion
The present study describes an astrocyte-mediated LTP of glutamatergic transmission to DA neurons in the VTA circuitry that we term
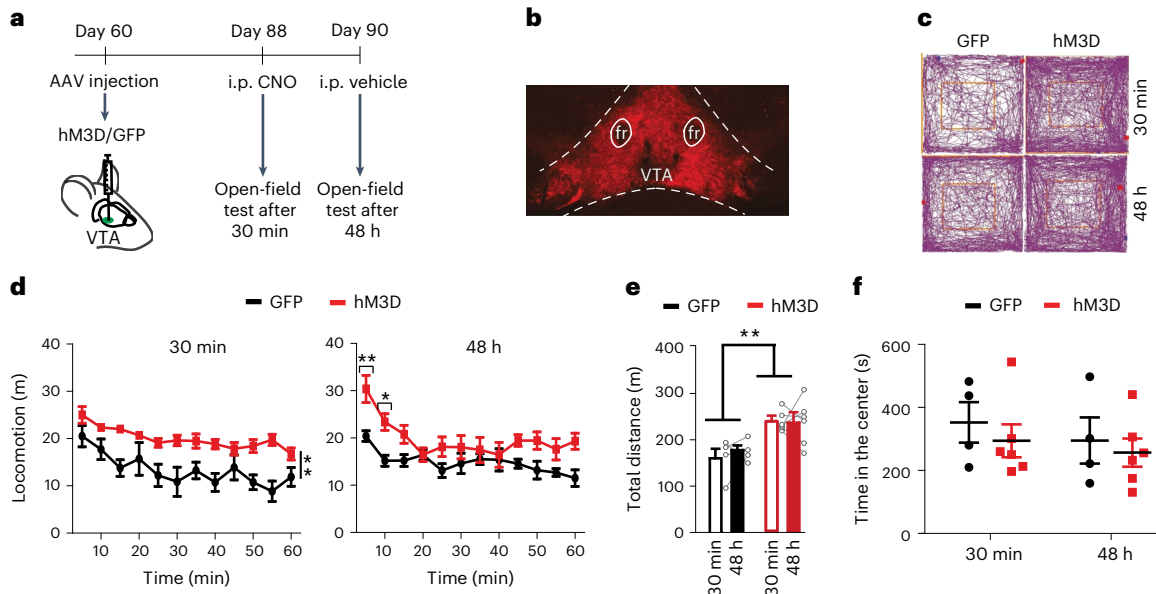
Fig. 6 | Chemogenetic activation in vivo of astrocytes induces a long-lasting motor hyperactivity. a, Schematic of the experimental design for testing locomotion in mice expressing either GFP or hM3D in VTA astrocytes, 30 minutes and 48 hours after i.p. CNO application (3 mg kg^{-1}). **b**, Fluorescence image of hM3D expression in VTA; fr, fasciculus retroflexus. **c**, Representative examples of locomotion in the open-field test. **d,e**, Locomotor activity (**d**) and total distance (**e**) traveled by GFP-injected and hM3D-injected mice 30 minutes or 48 hours after i.p. CNO injection (3 mg kg^{-1}; GFP group, n = 4 mice; hM3D group, n = 6 mice). Locomotor activity: 30 minutes, P = 0.08 for time × injection, P = 0.005 for virus, P < 0.0001 for time (two-way repeated-measures ANOVA);

48 hours, P = 0.01 for time × injection, P < 0.01 for 5-minute GFP versus hM3D, P < 0.05 for 10-minute GFP versus hM3D (two-way repeated-measures ANOVA and Bonferroni's multiple comparison test; main effects are not indicated). Total distance: P = 0.58 for time × virus, P = 0.005 for virus, P = 0.7 for time (two-way repeated-measures ANOVA). **f**, Time spent in the open-field center of GFP-injected and hM3D-injected mice (GFP group, n = 4 mice; hM3D group, n = 6 mice) at different timepoints after i.p. CNO injection. Two-way repeated-measures ANOVA: P = 0.73 for time × virus, P = 0.55 for virus, P = 0.13 for time. Data are represented as mean ± s.e.m.

bLTP. This novel form of synaptic plasticity is evoked by the following sequence of events (Fig. 7). First, DA neuron bursting activity induces the somatodendritic release of eCBs and DA; second, activation of CB1 and D2Rs in astrocytes triggers Ca^{2+} elevations; and third, astrocyte activation, coupled with another signal, possibly NO (Supplementary Note 2), released during DA neuron bursts, leads to an LTP of excitatory transmission onto adjacent DA neurons. At the basis of this potentation is the pre-synaptic activation of the mGluR1 receptor that mediates a sustained increase in glutamate release probability. We also show that in vivo astrocyte activation increases burst and overall firing activity of DA neurons and induces hyperlocomotion. These results indicate that astrocytes play a key role in the modulation of VTA DA neuron circuits that control DA-dependent physiological functions.

Astrocytes have been shown to respond with Ca^{2+} elevations to synaptic neurotransmitters and, in turn, to contribute to sensory information processing and behavioral responses[13–15,36–39]. We show here that, in the VTA, activation of both CB1 and D2Rs is required for astrocyte Ca^{2+} responses to DA neuron bursts and that these events are crucial for bLTP generation. This is based on the following observations: (1) CB1 and D2Rs are expressed and closely localized in the same astrocyte; (2) both astrocyte Ca^{2+} response and bLTP induction are abolished in the presence of specific antagonists that block either the CB1 or the D2R; (3) DA neuron bursts fail to evoke bLTP after deletion in VTA astrocytes of either the CB1 or the D2R; (4) bLTP could not be evoked after the impairment of astrocyte Ca^{2+} elevations downstream CB1 and D2R activation; and (5) in the presence of CB1 and D2R antagonists, bLTP can be induced in young male mice upon selective chemogenetic activation of astrocytes coupled to DA neuron bursts. Notably, the results reported above in (3)–(5) provide evidence that activation of neuronal CB1 and D2Rs is not required for bLTP induction.

It is worthwhile to further comment on results reported in (3). In our experiments on mice carrying the 'floxed' CB1 or D2 gene and injected in
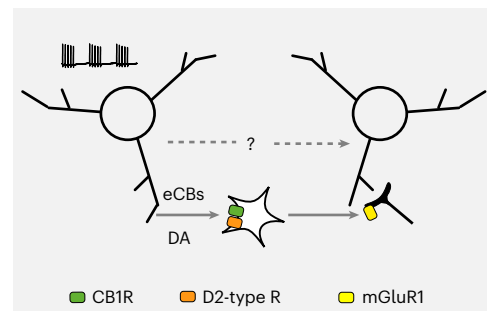
Fig. 7 | Proposed mechanism of bLTP generation. See text for details.

the VTA with AAV9/2-hGFAP-mCherry_iCre, we observed that the great majority of Cre$^+$ cells were astrocytes and only about 5% were neurons (Extended Data Fig. 7). However, this approach may lead to undetectable expression levels of the Cre recombinase and result in CB1 or D2R deletion in a higher percentage of neurons[40]. It is noteworthy, however, that neuronal CB1 and D2Rs in the VTA are inhibitory. Indeed, activation of pre-synaptic CB1 or D2Rs inhibits excitatory transmission onto VTA DA neurons[9,16], and activation of post-synaptic D2Rs induces a hyperpolarization that reduces VTA DA neuron excitability[9]. Furthermore, D2R activation in the VTA favors eCB-induced suppression of excitation[16]. These well-established inhibitory actions of neuronal CB1 and D2Rs in VTA circuitry are not consistent with the CB1 and D2R-dependent bLTP that we describe here and further support that activation of astrocytic, rather than neuronal, CB1 and D2Rs is required for bLTP generation.

Recent studies reported that astrocytes in different brain regions, including the VTA, express D1 and D2-type receptors and respond to bath-applied DA stimuli with complex Ca^{2+} dynamics, including regulation of basal cytosolic Ca^{2+} and repetitive Ca^{2+} transients[41–44].

Most interestingly, astrocytes in the NAc respond to synaptic DA release with D1R-mediated rather than D2R-mediated Ca^{2+} elevations[44]. These data confirm that astrocytes of different brain regions and synaptic circuits express different receptors that match the specific signals generated by distinct neuronal activities[13]. Consistent with this view, through the low-affinity D1R, NAc astrocytes can sense the transient, high DA concentrations generated by synaptic DA release[33]. Conversely, through the high-affinity D2R[33], VTA astrocytes can sense lower DA concentrations mainly generated in the VTA by somatodendritic rather than synaptic release and, thus, be functional targets of DA volume transmission[45] (Supplementary Note 1).

An additional specificity of VTA astrocytes is that a cooperativity between CB1 and D2Rs is necessary for the Ca^{2+} response to DA neuron bursts, being activation of either CB1 or D2Rs alone insufficient to induce astrocytic Ca^{2+} elevations. Our EM immunogold experiments provide an ultrastructural background for this cooperativity, revealing that CB1 and D2Rs are expressed in the same astrocytes, closely localized at astrocytic processes. Quantitative analysis from CB1/D2R double-labeled astrocytic processes also reveals that a group of couples exhibits an edge-to-edge separation ≤50 nm, which suggests physical interactions between CB1 and D2Rs and possible formation of heterodimers. Consistently, previous studies reported that D2 and CB1R co-activation in neurons enhances the formation of CB1/D2R heterodimers[17,46]. Furthermore, we recently showed that co-activation of GABA$_B$ and somatostatin receptors in neocortical astrocytes confers signaling specificity between different interneuron subtypes and astrocytes[47]. Although additional experiments are necessary to fully elucidate the mechanism by which the effect that we observe involves both D2 and CB1 receptors, a cooperativity between different G-protein-coupled receptors may, therefore, be a general functional feature of the astrocyte response to neuronal signals. Overall, CB1/D2R-expressing astrocytes in the VTA are fine-tuned to sense eCB and dopamine-releasing neurons and extent excitation to neighboring DA neurons through lateral potentiation of glutamatergic transmission. These results provide further evidence for circuit-specificity and synapse-specificity of neuron–astrocyte reciprocal signaling in the brain[13].

The astrocyte-mediated bLTP is absent in young male mice in which DA neuron bursts fail to elevate Ca^{2+} in astrocytes. Our data suggest that this failure is most likely due to a lower expression of astrocytic CB1Rs in young with respect to adult male mice showing regular bLTP. Notably, bLTP is observed in young male mice by coupling DA neuron bursts with Ca^{2+} elevations evoked by CNO in hM3D-expressing astrocytes. These results further support a crucial role of astrocytic Ca^{2+} signals in bLTP induction mechanism.

In hippocampus, dorsal striatum and neocortex, the somatodendritic release of eCBs recruits astrocytes that modulate synaptic transmission through pre-synaptic receptor activation[18–20,48]. In our VTA experiments, the presence of the mGluR1β at excitatory axon terminals, the significant changes in PPR and the CV values are also consistent with a pre-synaptic mechanism in bLTP mediated by mGluR activation (Supplementary Note 3). Different astrocytic actions could account for pre-synaptic mGluR modulation, including (1) glutamate release from activated astrocytes, (2) changes in astrocytic glutamate transporter activity that increase extracellular glutamate[49] or (3) rapid, structural rearrangement of astrocytic peri-synaptic processes expressing glutamate transporters[50]. Additional experiments are necessary to specifically address these different hypotheses.

Astrocytic Ca^{2+} signaling is required for bLTP generation in young and adult mice. However, although the mechanism downstream astrocyte Ca^{2+} signaling remains similar, IP$_3$R2 deletion in adult mice is insufficient to abolish bLTP, and, consistently, a Ca^{2+} response to DA neuron bursting is observed at astrocyte processes from IP$_3$R2$^{-/-}$ mice. This finding reveals an increased complexity in the regulatory mechanisms of astrocytic Ca^{2+} dynamics during development with contribution of signaling pathways other than the IP$_3$R2-mediated pathway in

IP$_3$R2$^{-/-}$ mice[27,51]. From these observations, it also follows that negative results on the role of astrocytic Ca^{2+} signaling in IP$_3$R2$^{-/-}$ adult mice must be interpreted with caution.

Transient and/or persistent potentiation of glutamatergic synapses, fundamentally mediated by NMDAR activation, regulates the burst firing mode of VTA DA neurons that plays a pivotal role in DA-dependent behaviors[1,33]. The novel form of astrocyte-mediated potentiation described here may integrate with these other forms of NMDAR-dependent plasticity that favor the burst firing of DA neurons. Consistent with this view, we report that in vivo astrocyte activation enhances DA neuron bursts and leads to a long-lasting locomotor hyperactivity that recent studies revealed to depend on VTA rather than SN DA neuron activity[3,34,35]. Although the molecular mechanism of astrocyte modulation of glutamatergic transmission, showed in brain slice preparations, is fully consistent with the results presented in Fig. 5, we cannot exclude that other processes, apart from the synaptic mechanism, can contribute to the effects observed in vivo. Additional experiments are necessary to specifically address this issue.

We suggest that activation of astrocytes by burst firing DA neurons and the consequent lateral potentiation of glutamatergic synapses may represent a strategy used by individual DA neurons to expand the burst firing mode to neighboring DA neurons. Hence, it is possible that, through the fundamental recruitment of astrocytes, an isolated, high-bursting DA neuron favors the formation of spatially defined clusters of co-active DA neurons that convey essential information about a specific subset of behavioral variables to target regions[52].

The present results show that astrocyte signaling induces a long-lasting potentiation of glutamatergic synapses to VTA DA neurons, induces a sustained increase in the burst firing mode of DA neurons and favors locomotor hyperactivity, thereby revealing an astrocyte-mediated mechanism in the control of DA neuron activity and DA-dependent behaviors. Our study also paves the way to future investigations examining whether dysregulations of DA neuron–astrocyte reciprocal communication within the VTA contribute to the development of disease states, including motivation disorders, psychiatric disorders with a strong motor component, such as attention-deficit/hyperactivity disorder, and drug addiction.

Online content

References

1. Pignatelli, M. & Bonci, A. Role of dopamine neurons in reward and aversion: a synaptic plasticity perspective. *Neuron* **86**, 1145–1157 (2015).
2. Thiele, A. & Bellgrove, M. A. Neuromodulation of attention. *Neuron* **97**, 769–785 (2018).
3. Runegaard, A. H. et al. Modulating dopamine signaling and behavior with chemogenetics: concepts, progress, and challenges. *Pharmacol. Rev.* **71**, 123–156 (2019).
4. Paladini, C. A. & Roeper, J. Generating bursts (and pauses) in the dopamine midbrain neurons. *Neuroscience* **282**, 109–121 (2014).
5. Morales, M. & Margolis, E. B. Ventral tegmental area: cellular heterogeneity, connectivity and behaviour. *Nat. Rev. Neurosci.* **18**, 73–85 (2017).
6. Poulin, J. F. et al. Mapping projections of molecularly defined dopamine neuron subtypes using intersectional genetic approaches. *Nat. Neurosci.* **21**, 1260–1271 (2018).
7. Beier, K. T. et al. Circuit architecture of VTA dopamine neurons revealed by systematic input–output mapping. *Cell* **162**, 622–634 (2015).

8. Watabe-Uchida, M., Zhu, L., Ogawa, S. K., Vamanrao, A. & Uchida, N. Whole-brain mapping of direct inputs to midbrain dopamine. *Neurons Neuron* **74**, 858–873 (2012).

9. Morikawa, H. & Paladini, C. A. Dynamic regulation of midbrain dopamine neuron activity: intrinsic, synaptic, and plasticity mechanisms. *Neuroscience* **198**, 95–111 (2011).

10. Bonci, A. & Malenka, R. C. Properties and plasticity of excitatory synapses on dopaminergic and GABAergic cells in the ventral tegmental area. *J. Neurosci.* **19**, 3723–3730 (1999).

11. Gomez, J. A. et al. Ventral tegmental area astrocytes orchestrate avoidance and approach behavior. *Nat. Commun.* **10**, 1455 (2019).

12. Octeau, J. C. et al. Transient, consequential increases in extracellular potassium ions accompany channelrhodopsin2 excitation. *Cell Rep.* **27**, 2249–2261 (2019).

13. Araque, A. et al. Gliotransmitters travel in time and space. *Neuron* **81**, 728–739 (2014).

14. Bazargani, N. & Attwell, D. Astrocyte calcium signaling: the third wave. *Nat. Neurosci.* **19**, 182–189 (2016).

15. Volterra, A., Liaudet, N. & Savtchouk, I. Astrocyte Ca^{2+} signalling: an unexpected complexity. *Nat. Rev. Neurosci.* **15**, 327–335 (2014).

16. Melis, M. et al. Endocannabinoids mediate presynaptic inhibition of glutamatergic transmission in rat ventral tegmental area dopamine neurons through activation of CB1 receptors. *J. Neurosci.* **24**, 53–62 (2004).

17. Busquets-Garcia, A., Bains, J. & Marsicano, G. CB1 receptor signaling in the brain: extracting specificity from ubiquity. *Neuropsychopharmacology* **43**, 4–20 (2018).

18. Navarrete, M. & Araque, A. Endocannabinoids potentiate synaptic transmission through stimulation of astrocytes. *Neuron* **68**, 113–126 (2010).

19. Gómez-Gonzalo, M. et al. Endocannabinoids induce lateral long-term potentiation of transmitter release by stimulation of gliotransmission. *Cereb. Cortex* **25**, 3699–3712 (2015).

20. Martín, R., Bajo-Grañeras, R., Moratalla, R., Perea, G. & Araque, A. Circuit-specific signaling in astrocyte–neuron networks in basal ganglia pathways. *Science* **349**, 730–734 (2015).

21. Wang, H. & Lupica, C. R. Release of endogenous cannabinoids from ventral tegmental area dopamine neurons and the modulation of synaptic processes. *Prog. Neuropsychopharmacol. Biol. Psychiatry* **52**, 24–27 (2014).

22. Rice, M. E. & Patel, J. C. Somatodendritic dopamine release: recent mechanistic insights. *Philos. Trans. R. Soc. B Biol. Sci.* **370**, 20140185 (2015).

23. Lalive, A. L. et al. Firing modes of dopamine neurons drive bidirectional GIRK channel plasticity. *J. Neurosci.* **34**, 5107–5114 (2014).

24. Lohani, S. et al. Burst activation of dopamine neurons produces prolonged post-burst availability of actively released dopamine. *Neuropsychopharmacology* **43**, 2083–2092 (2018).

25. Dahan, L. et al. Prominent burst firing of dopaminergic neurons in the ventral tegmental area during paradoxical sleep. *Neuropsychopharmacology* **32**, 1232–1241 (2007).

26. Srinivasan, R. et al. Ca^{2+} signaling in astrocytes from $Ip3r2^{-/-}$ mice in brain slices and during startle responses in vivo. *Nat. Neurosci.* **18**, 708–717 (2015).

27. Agarwal, A. et al. Transient opening of the mitochondrial permeability transition pore induces microdomain calcium transients in astrocyte processes. *Neuron* **93**, 587–605 (2017).

28. Serrano, A., Haddjeri, N., Lacaille, J. C. & Robitaille, R. GABAergic network activation of glial cells underlies hippocampal heterosynaptic depression. *J. Neurosci.* **26**, 5370–5382 (2006).

29. Lüscher, C. & Malenka, R. C. NMDA receptor-dependent long-term potentiation and long-term depression (LTP/LTD). *Cold Spring Harb. Perspect. Biol.* **4**, a005710 (2012).

30. Hardingham, N., Dachtler, J. & Fox, K. The role of nitric oxide in pre-synaptic plasticity and homeostasis. *Front. Cell. Neurosci.* **7**, 190 (2013).

31. Pasti, L., Pozzan, T. & Carmignoto, G. Long-lasting changes of calcium oscillations in astrocytes. A new form of glutamate-mediated plasticity. *J. Biol. Chem.* **270**, 15203–15210 (1995).

32. Yu, X. et al. Reducing astrocyte calcium signaling in vivo alters striatal microcircuits and causes repetitive behavior. *Neuron* **99**, 1170–1187 (2018).

33. Grace, A. A., Floresco, S. B., Goto, Y. & Lodge, D. J. Regulation of firing of dopaminergic neurons and control of goal-directed behaviors. *Trends Neurosci.* **30**, 220–227 (2007).

34. Boekhoudt, L. et al. Chemogenetic activation of dopamine neurons in the ventral tegmental area, but not substantia nigra, induces hyperactivity in rats. *Eur. Neuropsychopharmacol.* **26**, 1784–1793 (2016).

35. Jing, M. Y. et al. Re-examining the role of ventral tegmental area dopaminergic neurons in motor activity and reinforcement by chemogenetic and optogenetic manipulation in mice. *Metab. Brain Dis.* **34**, 1421–1430 (2019).

36. Nagai, J. et al. Behaviorally consequential astrocytic regulation of neural circuits. *Neuron* **109**, 576–596 (2021).

37. Kofuji, P. & Araque, A. Astrocytes and behavior. *Annu. Rev. Neurosci.* **44**, 49–67 (2021).

38. Martin-Fernandez, M. et al. Synapse-specific astrocyte gating of amygdala-related behavior. *Nat. Neurosci.* **20**, 1540–1548 (2017).

39. Adamsky, A. et al. Astrocytic activation generates de novo neuronal potentiation and memory enhancement. *Cell* **174**, 59–71 (2018).

40. Nagai, J. et al. Hyperactivity with disrupted attention by activation of an astrocyte synaptogenic cue. *Cell* **177**, 1280–1292 (2019).

41. Jennings, A. et al. Dopamine elevates and lowers astroglial Ca^{2+} through distinct pathways depending on local synaptic circuitry. *Glia* **65**, 447–459 (2017).

42. Xin, W. et al. Ventral midbrain astrocytes display unique physiological features and sensitivity to dopamine D2 receptor signaling. *Neuropsychopharmacology* **44**, 344–355 (2019).

43. Cui, Q. et al. Blunted mGluR activation disinhibits striatopallidal transmission in parkinsonian mice. *Cell Rep.* **17**, 2431–2444 (2016).

44. Corkrum, M. et al. Dopamine-evoked synaptic regulation in the nucleus accumbens requires astrocyte activity. *Neuron* **105**, 1036–1047 (2020).

45. Fuxe, K., Agnati, L. F., Marcoli, M. & Borroto-Escuela, D. O. Volume transmission in central dopamine and noradrenaline neurons and its astroglial targets. *Neurochem. Res.* **40**, 2600–2614 (2015).

46. Kearn, C. S., Blake-Palmer, K., Daniel, E., Mackie, K. & Glass, M. Concurrent stimulation of cannabinoid CB1 and dopamine D2 receptors enhances heterodimer formation: a mechanism for receptor cross-talk? *Mol. Pharmacol.* **67**, 1697–1704 (2005).

47. Mariotti, L. et al. Interneuron-specific signaling evokes distinctive somatostatin-mediated responses in adult cortical astrocytes. *Nat. Commun.* **9**, 82 (2018).

48. Min, R. & Nevian, T. Astrocyte signaling controls spike timing-dependent depression at neocortical synapses. *Nat. Neurosci.* **15**, 746–753 (2012).

49. Boender, A. J., Bontempi, L., Nava, L., Pelloux, Y. & Tonini, R. Striatal astrocytes shape behavioral flexibility via regulation of the glutamate transporter EAAT2. *Biol. Psychiatry* **89**, 1045–1057 (2020).

50. Henneberger, C. et al. LTP Induction boosts glutamate spillover by driving withdrawal of perisynaptic astroglia. *Neuron* **108**, 919–936 (2020).

51. Shigetomi, E., Jackson-Weaver, O., Huckstepp, R. T., O'Dell, T. J. & Khakh, B. S. TRPA1 channels are regulators of astrocyte basal calcium levels and long-term potentiation via constitutive D-serine release. *J. Neurosci.* **33**, 10143–10153 (2013).

52. Engelhard, B. et al. Specialized coding of sensory, motor and cognitive variables in VTA dopamine neurons. *Nature* **570**, 509–513 (2019).

Publisher's note Springer Nature remains neutral with regard to jurisdictional claims in published maps and institutional affiliations.

Methods

Animals and brain slice preparation

Animal care, handling and procedures were carried out in accordance with national (D.L. n.26, 14 March 2014) and European Community Council (2010/63/UE) laws, policies and guidelines and were approved by the Italian Ministry of Health (D2784.N.TU2/2018; 40A31.N.ZUK, 754/2018-PR, 749/2017-PR and 639/2020-PR) and by the local Institutional Animal Care and Use Committees of the Università di Padova, Università Politecnica delle Marche and Istituto Italiano di Tecnologia. Mice were housed under a 12-hour light/dark cycle (7:00–19:00 light), with a room temperature of 22 °C and humidity of 60%. Horizontal VTA slices (240 μm) were obtained from both male and female C57BL/6J WT mice and inositol 1,4,5-triphosphate-type 2 receptor (IP$_3$R2) knockout mice (IP$_3$R2$^{-/-}$)[53] and from male $Cnr1$-flox[54] and $Drd2$-flox[55] mice, at P14–17 (young mice) or P30–70 (adolescent/adult mice). Polymerase chain reaction (PCR) was used to periodically genotype the different mouse lines (forward and reverse primers; IP3 WT: ACCCTGATGAGG-GAAGGTCT and ATCGATTCATAGGGCACACC; IP3 mutant: AATGGGCT-GACCGCTTCCTCGT and TCTGAGAGTGCCTGGCTTTT; $Cnr1$-floxed: GCTGTCTCTGGTCCTCTTAAA and GGTGTCACCTCTGAAAACAGA; and $Drd2$-floxed: TCTCCCTCATCTCTGGACTCA and TGGGAAAGGGCTACA-GCA). Because of the mixed genetic background of the IP$_3$R2$^{-/-}$ mice (Black Swiss, 129 and C57BL/6J)[53], we also performed experiments in IP$_3$R2$^{-/-}$ and IP$_3$R2$^{+/+}$ littermates obtained after crossing C57BL/6J WT mice with IP$_3$R2$^{-/-}$ mice (Extended Data Fig. 2). Separated data from adult non-littermate and littermate mice are reported in Extended Data Fig. 10. Given that results obtained from these groups were similar, data from adult mice were pooled together in Fig. 4. For slice preparations, animals were anesthetized with isofluorane, and the brain was removed and transferred into an ice-cold artificial cerebrospinal fluid (ACSF) containing (in mM): 125 NaCl, 2 KCl, 2 CaCl$_2$, 1 MgCl$_2$, 25 glucose, 25 NaHCO$_3$ and 1.25 NaH$_2$PO$_4$, pH 7.4, with 95% O$_2$/5% CO$_2$. Slices were cut with a vibratome (Leica, VT1000S) in the ice-cold solution described in Dugué et al.[56] containing (in mM): 130 K-gluconate, 15 KCl, 0.2 EGTA, 20 HEPES, 25 glucose and 2 kynurenic acid. Slices were then transferred for 1 minute in a room temperature solution containing (in mM): 225 D-mannitol, 2.5 KCl, 1.25 NaH$_2$PO$_4$, 26 NaHCO$_3$, 25 glucose, 0.8 CaCl$_2$ and 8 MgCl$_2$, with 95% O$_2$/5% CO$_2$. Finally, slices were transferred in ACSF at 32 °C for 15–20 minutes and then maintained at room temperature for the entire experiment.

Electrophysiological recordings and extracellular stimulation

Brain slices were continuously perfused in a submerged chamber with recording solution containing (in mM): 120 NaCl, 2 KCl, 1 NaH$_2$PO$_4$, 26 NaHCO$_3$, 1 MgCl$_2$, 2 CaCl$_2$, 10 glucose, pH 7.4 (with 95% O$_2$/5% CO$_2$). Picrotoxin (50 μM) was added to block GABA$_A$ receptor currents. When indicated, other antagonists were bath-applied with the recording solution. Cells were visualized with an Olympus FV1000 microscope (Olympus Optical). Conventional VTA DA neurons were recorded in the lateral part of the region medial to the medial terminal nucleus of the accessory optical tract (Fig. 1)[5,57]. DA neurons from the lateral VTA were identified on the basis of their distinct morphology characterized by a large and elongated soma with no particular dendritic orientation and the presence of the following electrophysiological properties: a low-frequency tonic firing, a large I$_h$ current elicited by hyperpolarizing steps[16] and a slow depolarizing potential during current step injections[58] (Extended Data Fig. 1b–d). Simultaneous electrophysiological whole-cell patch-clamp recordings from two DA neurons were made (distance of the somata, 70–120 μm; this distance was used in previous studies that revealed astrocyte-mediated lateral potentiation[18], and it is consistent with the territory occupied by individual astrocytic processes, which has a diameter of 80–100 μm[59]). Patch electrodes for neuronal recordings (resistance, 3–4 MΩ) were filled with an internal solution containing (in mM): 135 K-gluconate, 70 KCl, 10 HEPES, 1 MgCl$_2$ and 2 Na$_2$ATP (pH 7.4, adjusted with KOH, 280–290 mOsm L^{-1}).

Recordings were obtained using a multiclamp-700B amplifier (Molecular Devices). Signals were filtered at 1 kHz and acquired at 10-kHz sampling rate with a DigiData 1440A interface board and pClamp 10 software. Series and input resistances were monitored throughout the experiment using a 5-mV pulse. Recordings were considered stable when the change of series and input resistances were below 20%. Cells that did not meet these criteria were discharged. Theta capillaries filled with recording solution were used for bipolar stimulation. To stimulate glutamatergic afferents, electrodes were connected to an S-900 stimulator through an isolation unit and placed 100–200 μm rostral to the recording electrode (Extended Data Fig. 1a). Paired pulses (50-ms intervals) were delivered at 0.33 Hz. EPSCs were recorded while holding the membrane potential at −70 mV. Stimulus intensity was adjusted to evoke 30–50% maximal EPSC amplitude. The EPSC amplitude was measured as the peak current amplitude (2–9 ms after stimulus) minus the mean baseline current (100 ms before stimulus). To illustrate the mean EPSCs time course, values were grouped in 3-minute bins (that is, mean EPSCs from 60 stimuli). Changes in mean EPSCs in the first DA neuron were monitored after imposing a burst or a tonic firing pattern to the second DA neuron (70–120 μm apart). Burst firing pattern was imposed in current-clamp mode, through injections of intracellular current pulses, five pulses at 20 Hz every 500 ms for 5 minutes (Extended Data Fig. 1e)[23]. Tonic firing was imposed with individual current pulses applied at 2 Hz for 5 minutes[23] (Extended Data Fig. 1e). During the burst/tonic firing, the extracellular stimulation was switched off. In electrophysiological experiments, time 0 indicates the end of the burst/tonic firing. For statistical analysis of long-term effects, mean EPSCs from 120 stimuli applied before (basal), 24–30 minutes (indicated as 30-minute timepoint in the bar chart) or 39–45 minutes (indicated as 45-minute timepoint in the bar chart) after the firing protocol were compared. In young adult mice, only the long-term effect at the timepoint of 30 minutes was analyzed owing to the difficulty of obtaining long-lasting recordings in tissues from these mice. PPR was calculated as 2nd EPSC/1st EPSC, and evaluation of the PPR before (mean value from two basal recordings) and after (mean value from recordings at 39 minutes and 45 minutes, indicated as 45 minutes) the burst firing protocol was used to identify the pre-synaptic or post-synaptic locus of the bLTP. For the analysis of the CV (CV = σ/μ) of the EPSCs, we divided the standard deviation (σ) by the mean (μ) of 120 evoked EPSCs before and 39–45 minutes (indicated as $_{45min}$ timepoint) after the burst firing protocol for each potentiated cell. Then, we calculated (CV$^{-2}_{45min}$ normalized)/mean$_{45min}$ normalized for each cell. Values of ((CV$^{-2}_{45min}$ norm)/mean$_{45min}$ norm) > 1 support a pre-synaptic locus of plasticity expression[60]. For BAPTA dialysis into the astrocyte syncytium, we used a patch pipette (5–6 MΩ) containing (in mM): 50 BAPTA-tetrapotassium, 2 ATP.Na, 0.4 GTP.Na, 10 HEPES, 10 phosphocreatine.Na, 20 KMeSO$_3$, 3 ascorbic acid, 1 MgCl$_2$, 8 NaCl and 0.06 Alexa Fluor 594 (pH 7.3, adjusted with KOH, 270–290 mOsm L^{-1}, modified from ref. [28]). Astrocyte identity was verified by passive response to square current injections in current clamp. To avoid a leakage of BAPTA from the pipette during seal formation, the BAPTA solution was backfilled after loading the tip with a standard intracellular solution. Dialysis of fluorescence marker was monitored 40–50 minutes after the whole-cell configuration.

Ca^{2+} imaging experiments

Slices from young mice were loaded with the astrocyte-specific marker Sulforhodamine 101 (SR101) (0.3 μM, Sigma-Aldrich) in ACSF at 32 °C for 15 minutes. Then, slices were loaded for 45 minutes at room temperature with the Ca^{2+}-sensitive dye Fluo4-AM (7.6 μM, Thermo Fisher Scientific) in an ACSF solution containing pluronic F-127 (0.0067%, Sigma-Aldrich) and bubbled with 95% O$_2$/5% CO$_2$. Ca^{2+} imaging experiments were conducted with a confocal laser scanning microscope (TCS-SP5-RS, Leica Microsystems) equipped with two solid-state lasers tuned at 448 nm and 543 nm (to image Fluo-4 and SR101 fluorescence, respectively) and a ×20 objective (NA 1.0). Images (8-bit

depth) were acquired with a 0.5-Hz frame rate for 90 seconds, with time intervals of 5 minutes between recordings. Image sequences were processed with ImageJ software. Regions of interest (ROIs) were drawn around cellular somata using the red SR101 signal. Ca^{2+} events were estimated as changes of the Fluo-4 fluorescence signal over baseline ($\Delta F/F_0 = (F(t)-F_0)/F_0$). A fluorescence increase was considered an event when it exceeded two times the standard deviation from the baseline. Astrocyte Ca^{2+} responses were quantified by analyzing the probability of occurrence of Ca^{2+} spike by detecting the onset of Ca^{2+} elevations (Ca^{2+} spikes) during the recording period. To investigate the astrocyte response to the burst firing of DA neurons, a DA neuron was patched with an intracellular solution (see details before) containing the fluorescent tracer Neurobiotin 488 (60 µM, Vector Laboratories) to visualize neuronal soma and dendrites. To obtain the time course of the Ca^{2+} spike probability index reported in Figs. 1 and 2, the number of astrocytic Ca^{2+} spikes for each recording period was divided by the number of SR101+ astrocytes in proximity (around 50 µm) to Neurobiotin 488-filled DA neuron soma and dendrites. After three basal recordings, a burst firing pattern was imposed to the DA neuron (in current-clamp mode, through injections of intracellular current pulses, with five-pulse 20-Hz burst every 500 ms for 5 minutes), and the quantification of the Ca^{2+} spike probability was resumed 4.5 minutes after the initiation of the burst firing. In Ca^{2+} imaging experiments, time 0 indicates the onset of the burst firing. For statistical analysis, a mean value of the Ca^{2+} spike probability per minute per slice was calculated at basal conditions (mean of the three basal recordings) and after DA neuronal burst firing (mean of four consecutive recordings after the burst firing, the first at a timepoint of 4.5 minutes after the burst firing and the last at a timepoint of 24 minutes after the burst firing). To analyze the astrocyte response to D1R activation in young female mice, the D1-type receptor agonist SKF 38393 (1 mM) was locally delivered to SR-101 and Fluo-4 loaded VTA slices by using a pressure ejection unit (PDSE, NPI Electronics) that applies pulses (0.5 bar, 2 seconds) to a SKF 38393-containing pipette. Astrocyte Ca^{2+} responses in the presence of TTX (1 µM) were quantified analyzing the Ca^{2+} spike probability in 10-second bins. A mean time course of the Ca^{2+} spike probability per slice was calculated at basal conditions and after SKF 38393 challenge, from three recordings in each condition (5-minute intervals between recordings). The mean time course of the Ca^{2+} spike probability for all the experiments is reported in Extended Data Fig. 3. For statistical analysis, the mean Ca^{2+} spike probability per minute was calculated at basal conditions and in the 10-second bin immediately after the SKF 38393 challenge. These experiments were performed in the absence or presence of the D1R antagonist SCH-23390 (10 µM). At the end of the recording session, ATP (4 mM) was locally delivered, and the Ca^{2+} spike probability in response to this agonist was calculated. When indicated, Ca^{2+} imaging experiments were performed in slices from young mice expressing the genetically encoded Ca^{2+} indicator cytoGCaMP6f and the Gq-protein-coupled DREADD hM3D in astrocytes (for AAV delivery details, see below). In these experiments, Ca^{2+} elevations were evoked by bath perfusion of the hM3D agonist CNO (10 µM). When CNO was coupled with DA neuron burst, CNO bath perfusion initiated 2.5 minutes after the start of the burst firing. A mean time course of the Ca^{2+} response to CNO was calculated by plotting the $\Delta F/F_0$ of an ROI drawn around the entire recording field. Then, plots were aligned for the Ca^{2+} peak to calculate the mean time course of the Ca^{2+} response to CNO. In adult male mice, Ca^{2+} signals were studied in GCaMP6f and tdTomato co-expressing astrocytes (for AAV delivery details, see below). Calcium imaging experiments in brain slices were performed using a two-photon laser scanning microscope (Multiphoton Imaging System, Scientifica) equipped with a pulsed red laser (Chameleon Ultra 2, Coherent). Power at sample was 10–17 mW. GCaMP6f and tdTomato were excited at 920 nm. Images (12-bit depth) were acquired with a water-immersion lens (Olympus, LUMPlan FI/IR ×20, 1.05 NA), with a field of view of 120 × 120 µm at 1.5-Hz acquisition frame rate. Calcium

signal recordings were performed for 2 minutes with 5-minute time intervals. To investigate the astrocyte response to the burst firing of DA neurons, a DA neuron was patched with an intracellular solution containing the fluorescent tracer Alexa Fluor 594 (60 µM, Vector Laboratories), which allows visualization of neuronal soma and dendrites at 800 nm. After three basal recordings, a burst firing pattern was imposed to the DA neuron (in current-clamp mode, through injections of intracellular current pulses, five pulses at 20 Hz every 500 ms for 5 minutes), and the Ca^{2+} signal recordings were resumed 4.5 minutes after the initiation of the burst firing. In these experiments, time 0 indicates the onset of the burst firing. To extract Ca^{2+} event dynamics at astrocyte processes from the entire field of view in an automated, unbiased, event-based way, we used AQuA[61]. Analysis of Ca^{2+} signals at the level of soma was performed by drawing ROIs around cellular somata using the red tdTomato signal. Then, Ca^{2+} events were identified with ImageJ and a custom software developed in MATLAB 7.6.0 R2008A (MathWorks) that essentially combines a threshold measured from the global baseline with a stricter threshold computed from a local baseline (for details, see ref. [47]). For statistical analysis, the mean value of the number of events per minute at processes and the number of events per minute per soma were calculated at basal conditions (mean of the three basal recordings) and after DA neuronal burst firing (mean of four consecutive recordings after the burst firing, the first at a timepoint of 4.5 minutes after the burst firing onset and the last at a timepoint of 25.5 minutes after the burst firing onset). The area, amplitude ($\Delta F/F_0$) and duration (from 10% onset time to 10% offset time) of Ca^{2+} events extracted by AQuA at basal conditions and after the burst firing were compared using the Kolmogorov–Smirnov test.

AAV delivery

We used graduated glass pipettes to bilaterally microinject in the VTA of C57BL/6J WT male mice, at P0–2 or P28–30, the viral vector ssAAV-9/2-hGFAP-hM3D(Gq)_mCherry-WPRE-hGHp(A) (VVF-UZH, $4.6 × 10^{12}$ viral genomes per milliliter (vg ml^{-1})) containing the astrocytic promoter GfaABC1D to selectively express in astrocytes the mCherry-tagged, Gq-coupled DREADD hM3D. Two to three weeks after microinjection, we performed electrophysiological experiments in brain slices from juvenile mice (P14–17) and in vivo single-unit recordings in adult mice (P45–50). As control for single-unit recording experiments, in the VTA of WT male mice we bilaterally injected the viral vector AAV5.GfaABC1D.cyto-tdTomato.SV40 (Addgene, $2.4 × 10^{13}$ vg ml^{-1}), which carries the astrocytic promoter GfaABC1D, to express selectively in astrocytes the tdTomato marker. In a group of P0–P2 mice, both ssAAV-9/2-hGFAP-hM3D(Gq)_mCherry-WPRE-hGHp(A) and AAV5.GfaABC1D.cytoGCaMP6f.SV40 (Addgene, $1.81 × 10^{13}$ genome copies per milliliter; pZac2.1 gfaABC1D-cyto-GCaMP6f was a gift from Baljit Khakh[62]) viral vectors were injected together to assess the Ca^{2+} responses evoked in astrocytes after activation of hM3D, using the Ca^{2+} indicator GCaMP6f. To selectively express the Cre recombinase in astrocytes, injections of the viral vector ssAAV9/2-hGFAP-mCherry_iCre-WPRE-hGHp(A) (VVF-UZH, $5.2 × 10^{12}$ vg ml^{-1}) carrying the astrocytic promoter GfaABC1D were bilaterally performed in the VTA of P28–30 male mice containing the *Drd2* or the *Cnr1*-floxed gene. As control mice, the same viral vector was injected in age-matched C57BL/6J WT mice. Brain slice electrophysiological experiments were performed 4 weeks after injection. IP$_3$R2$^{+/+}$ and IP$_3$R2$^{-/-}$ male mice, at P28–30, were bilaterally injected in the VTA with AAV5.GfaABC1D.cytoGCaMP6f.SV40 (Addgene, $1.81 × 10^{13}$ genome copies per milliliter) and AAV5.GfaABC1D.cyto-tdTomato.SV40 (Addgene, $2.4 × 10^{13}$ vg ml^{-1}), and, 2–3 weeks after injection, VTA slices were prepared to investigate in these mice the astrocyte response to DA neuron burst firing. AAV5.GfaABC1D.mCherry.hPMCA2w/b.SV40 (Penn Vector Core, $1.14 × 10^{13}$ genome copies per milliliter) was bilaterally injected in the VTA of both female and male IP$_3$R2$^{-/-}$ mice, at P28–30, to selectively express in astrocytes the Ca^{2+} pump hPMCA2w/b[32]. Brain slice electrophysiological experiments

were performed 4 weeks after injection. AAV5.GfaABC1D.mCherry.hPMCA2w/b.SV40 was injected without previous dilution. The other viral vectors were diluted to 50% in ACSF before injection. When two viral vectors were injected, both vectors were present at a 1:1 ratio, except for the injection of AAVs to express GCaMP6f and tdTomato in adult mice, in which a 0.6:0.4 ratio was used. The coordinates for viral injections were (in mm): AP 0.1, ML ± 0.15, DV −3.8 from lambda for P0–2 mice; AP −3.0, ML ± 0.5, DV −4.4 from bregma for P28–30 mice. For microinjections in P0 mice, animals were anesthetized by hypothermia for 3 minutes and fixed into a modeled platform. Using a manually graduated pulled glass pipette connected to a custom-made pressure injection system, we punched the skull bilaterally and injected a total volume of 350 nl containing the viral vector. After microinjection, the skin was sutured, and mice were revitalized under a heat lamp before returning to their cage. For injections in P28–30 mice, animals were anesthetized with isoflurane (induction 4–5%, maintenance 1–2%). Depth of anesthesia was assured by monitoring respiration rate, eyelid reflex, vibrissae movements and reactions to pinching the tail and toe. After drilling two holes into the skull over the VTA, we bilaterally injected a total volume of 500 nl per hole by using a pulled glass pipette connected to a peristaltic pump, at a rate of 100 nl min⁻¹. To express GCaMP6f and tdTomato in VTA astrocytes from adult mice, we injected a total volume of 1 µl by using a pulled glass pipette connected to a custom-made pressure injection system. To minimize AAV spreading along the pipette track, in adult mice injections the pipette was kept in the tissue for 10 minutes before slow withdrawal. The spreading to overlying tissue needs to be considered in all studies employing microinjections in subcortical brain regions and subsequent in vivo experiments[40], whereas this can be hardly a concern for the studies using horizontal brain slice preparations. After injections, the skin was sutured, and mice were revitalized under a heat lamp and returned to their cage.

VTA microinjections are astrocyte selective for the expression of the AAV-coded proteins (Results) and fundamentally restricted to the VTA. Some AAV spreading in surrounding VTA tissue is occasionally observed, mainly in young mice. In these latter mice, however, we limited our study to horizontal brain slice preparations where neural circuits and glutamatergic inputs are highly isolated and pharmacologically controlled (that is, experiments were performed in the presence of the GABA$_A$R antagonist picrotoxin). Furthermore, given the maximal length of astrocytic processes of about 50 µm, possible mistargeted astrocytes in regions outside the VTA, such as the SN, might affect the glutamatergic inputs to VTA DA neurons at the SN–VTA border, but they could not reach the lateral VTA region where pair recordings were performed.

Immunohistochemistry and cell counting

For the evaluation of the number of mCherry-expressing astrocytes and neurons, we prepared 70-µm-thick brain slices from young and adult animals injected with ssAAV-9/2-hGFAP-hM3D(Gq)_mCherry-WPRE-hGHp(A), ssAAV9/2-hGFAP-mCherry_iCre-WPRE-hGHp(A) or AAV5.GfaABC1D.mCherry.hPMCA2w/b.SV40. Mice were euthanized with 5% isoflurane and transcardially perfused with PBS, followed by ice-cold 4% paraformaldehyde in PBS. Brains were removed and post-fixed overnight at 4 °C in the same fixative solution. Horizontal brain slices were obtained with a VT1000S vibratome (Leica), collected as floating sections and blocked for 1 hour in the Blocking Serum (BS: 1% BSA, 2% goat serum and 1% horse serum in PBS) and 0.2% Triton X-100. After blocking, sections were incubated (overnight at 4 °C) with the following primary antibodies in BS plus 0.02% Triton X-100: anti-NeuN (RRID: AB_2298772, 1:200 mouse, Thermo Fisher Scientific/Millipore MAB377), anti-glial fibrillary acidic protein (GFAP, RRID: AB_10013382, 1:400 rabbit, Dako Agilent, Z0334), anti-S100β (RRID: AB_2315306, 1:400 rabbit, Dako Agilent, Z031129) and anti-glutamate transporter 1 (GLT1, RRID: AB_90949, 1:400 guinea

pig, Abcam, AB1783), pre-fixed in 50% methanol in PBS for 15 minutes. After washing with PBS, slices were incubated for 2 hours at room temperature with secondary antibodies conjugated with Alexa Fluor 488 (1:500; A21202 donkey anti-mouse; A21206 donkey anti-rabbit; A11073 goat anti-guinea pig, Invitrogen, Thermo Fisher Scientific). To evaluate mCherry⁺ cells, we directly evaluated the red fluorescence of infected slices. Only for IP$_3$R2$^{-/-}$ mice injected with AAV5.GfaABC1D.mCherry.hPMCA2w/b.SV40, we performed double immunofluorescence of NeuN (or GLT1) together with anti-RFP (RRID: AB_2209751, 1:1,000 rabbit, Rockland, 600-401-379). In this case, secondary antibodies were anti-mouse (or anti-guinea pig) Alexa Fluor 488 conjugated together with anti-rabbit Alexa Fluor 555 conjugated (A21430 donkey anti-rabbit, Invitrogen, Thermo Fisher Scientific, 1:500). We used the same experimental procedure to obtain horizontal VTA slices from adult mice injected with AAV5.GfaABC1D.cytoGCaMP6f.SV40. To evaluate the number of GCaMP6f-expressing astrocytes and neurons, we performed double immunofluorescence with anti-NeuN (RRID: AB_2298772, 1:200 mouse, Thermof Fisher Scientific/Millipore, MAB377) or anti-S100β (RRID: AB_2620025, 1:300 guinea pig, Synaptic Systems, 287004) antibodies plus donkey immunoglobulins anti-mouse Alexa Fluor 556 conjugated (RRID: AB_2534012, 1:500, Thermo Fisher Scientific, A10036) or goat anti-guinea pig Alexa Fluor 546 conjugated (RRID: AB_2534118, 1:500, Thermo Fisher Scientific, A11074), respectively. After secondary antibody incubation, we saturated with rabbit immunoglobulins and then performed the overnight incubation with the directly Alexa Fluor 488 conjugated rabbit polyclonal anti-GFP (Thermo Fisher Scientific, A21311, AB_221477) to identify GCaMP6-expressing cells. Slices were then washed, and nuclei were stained with Top-Ro3 (Invitrogen, Thermo Fisher Scientific, 1:1,000). Negative controls were performed in the absence of the primary antibodies. We used a TCS-SP5-RS laser scanning microscope (Leica, ×20, NA 1×/W objective) to acquire sequential three channels, confocal image z-stacks (1-µm z-step, 456.33 × 456.33 µm) and ImageJ for double-labeled cell counting. We counted mCherry⁺ cells, and then we evaluated the percentage of mCherry⁺ cells that were neurons (mCherry⁺/NeuN⁺) or glial cells. VTA from both hemispheres of injected animals were evaluated in 3–5 mice for each group.

Pre-embedding and post-embedding EM

Thirteen P16 and eight P50 C57BL/6 mice (seven females and six males for P16; four females and four males for P50) were used. Mice were anesthetized with an i.p. injection of chloral hydrate (300 mg kg⁻¹) and perfused transcardially with a flush of saline solution, followed by 4% freshly depolymerized paraformaldehyde and 0.2% glutaraldehyde in 0.1 M phosphate buffer (PB, pH 7.4). Brains were removed, post-fixed in the same fixative (for 48 hours) and cut on a vibratome in 50-µm serial horizontal sections from the midbrain, which were collected in PB until processing[63]. Horizontal sections were through the dorso-ventral extent of the VTA, resulting in 7–8 sections per series. To verify the dorso-ventral extension of VTA, a pilot series of sections from a male mouse were immuno-processed for tyrosine-hydroxylase (primary antibodies from Millipore, AB1542, RRID:AB_90755 (ref. [64]); 1:500) and for Nissl staining. In immuno-reacted sections (see 'Data collection and data analysis' section), lateral VTA was identified as the region medial to the medial terminal nucleus of the accessory optical tract[5,57].

Immunoperoxidase and pre-embedding procedures. Sections were treated with H$_2$O$_2$ (1% in PB, 30 minutes) to remove endogenous peroxidase activity, rinsed in PB and pre-incubated in 10% normal goat serum (NGS, 1 hour, for mGLUR1α, mGlur1β, D2, D3, D4 and D1) or in 10% normal donkey serum (NDS, 1 hour, for CB1). Sections were then incubated in a solution containing primary antibodies (see Supplementary Table 7 for dilutions, 2 hours at room temperature and overnight at 4 °C). The next day, sections were rinsed three times in PB and incubated first in 10% NGS or 10% NDS (15 minutes) and then in a solution containing secondary biotinylated secondary antibodies

(see Supplementary Table 7 for dilutions, 1.5 hours at room temperature). Sections were subsequently rinsed in PB, incubated in avidin-biotin peroxidase complex (ABC Elite, PK6100, Vector Laboratories), washed several times in PB and incubated in 3,3'diaminobenzidine tetrahydrochloride (DAB; 0.05% in 0.05 M Tris buffer, pH 7.6 with 0.03% H_2O_2). Method specificity was verified by substituting primary antibodies with PB or NGS. As previously described[63], after completion of immunoperoxidase procedures, sections were post-fixed in 1% osmium tetroxide in PB for 45 minutes and contrasted with 1% uranyl acetate in maleate buffer (pH 6.0, 1 hour). After dehydration in ethanol and propylene oxide, sections were embedded in Epon/Spurr resin (Electron Microscopy Sciences), flattened between Aclar sheets (Electron Microscopy Sciences) and polymerized at 60 °C for 48 hours. Chips including lateral VTA were selected by light-microscopic inspection, glued to blank epoxy and sectioned with an ultramicrotome (MTX, Arizona Research and Manufacturing Company). The most superficial ultrathin sections (~60 nm) were collected and mounted on 300 mesh nickel grids, stained with Sato's lead and examined with Philips EM 208 and CM10 electron microscopes coupled to a MegaView 2 high-resolution CCD camera (Olympus Soft Imaging Solutions). To minimize the effects of procedural variables, all material from P16 and P50 females and males was processed in parallel.

Post-embedding procedures. Sections were processed for an osmium-free embedding method[65]. Dehydrated sections were immersed in propylene oxide, infiltrated with a mixture of Epon/Spurr resins, sandwiched between Aclar films and polymerized at 60 °C for 48 hours. After polymerization, chips were cut from the wafers, glued to blank resin blocks and sectioned with an ultramicrotome. Thin sections (60–80 nm) were cut and mounted on 300 mesh nickel grids and processed for immunogold labeling[65,66]. In brief, after treatment with 4% para-phenylenediamine in Tris-buffered saline (0.1 M Tris, pH 7.6, with 0.005% Tergitol NP-10 (TBST)), grids were washed in TBST (pH 7.6), transferred for 15 minutes in 0.25% NDS in TBST (pH 7.6) and then incubated overnight (26 °C) in a solution of TBST (pH 7.6) containing a mixture of anti-D2 and anti-CB1 primary antibodies (see Supplementary Table 7 for dilutions). Grids were subsequently washed in TBST (pH 8.2), transferred for 10 minutes in 0.5% NDS in TBST (pH 8.2), incubated for 2 hours (26 °C) in TBST (pH 8.2) containing secondary antibodies conjugated to 18-nm and 12-nm gold particles, washed in distilled water and then stained with uranyl acetate and Sato's lead. The optimal concentration of antibodies to D2 and CB1Rs was sought by testing several dilutions; the concentration yielding the lowest level of background labeling and still immunopositive elements was used to perform the final studies. Gold particles were not detected when primary antiserum was omitted. When normal serum was substituted for immune serum, sparse and scattered gold particles were observed, but they did not show any specific relationship to subcellular compartments.

Data collection and analysis. All data were obtained from lateral VTA of immuno-reacted sections[5,57]. For pre-embedding EM, mGluR1α, mGluR1β, CB1, D1, D2, D3 and D4R immuno-reactive profiles were studied in ultrathin sections from the surface of the embedded blocks. Quantitative data derive from the analysis of microscopic fields of lateral VTA (10–12 ultrathin sections per animal) that were selected and captured at original magnifications of ×12,000–×30,000. Microscopical fields from females and males containing positive processes were randomly selected. Acquisition of microscopical fields and analysis of female and male mice were performed under blinded conditions.

For the analysis of the distribution of mGluR1α, mGluR1β, CB1, D1, D2, D3 and D4R positive profiles, subcellular compartments were identified according to well-established criteria[67] (Extended Data figures and Supplementary Tables 1, 3 and 4). For quantifying mGluR1α or mGluR1β in P16 VTA and mGluR1β in P50 VTA at axon terminals, synapses exclusively characterized by a pre-synaptic terminal with clear and round vesicles nearby the pre-synaptic density, by a synaptic cleft displaying electron dense material, by pre-synaptic and post-synaptic membranes defining the active zone and the post-synaptic specialization and, finally, by a prominent post-synaptic density, the asymmetric synapses[67,68] were sampled (axon terminals making asymmetric synaptic contacts containing one or more dense core vesicles more likely representative of co-release of glutamate and others neurotransmitters[69–71] were not included in this group; Supplementary Tables 2 and 6).

For quantifying CB1, D1, D2, D3 and D4R at astrocytic processes in P16 VTA and CB1 and D2R in P50 VTA, astrocytic profiles were identified based on their typical irregular outlines and the paucity of cytoplasmic components (with the exception of ribosomes, glycogen granules and various fibrils[67]). For post-embedding EM, ultrathin sections (20 ultrathin sections per animal) were examined at ×50,000–×85,000, and fields that included at least one double immuno-labeled astrocytic profile were selected. For determining the relative density of D2 and CB1Rs at the membranes of double-labeled astrocytic profiles, pyramidal cell nuclei were also identified: gold particles within labeled structures were counted, and areas were calculated using ImageJ. Background was calculated by estimating labeling density over pyramidal cell nuclei[66,72]. Particle densities were counted and compared with background labeling. Gold particles were considered associated with plasma membrane if they were within 20 nm of the extracellular side of the membrane. To determine the degree of nearness of D2 and CB1R at the membrane of double-labeled profiles, the edge-to-edge distances between immunogold-labeled D2 and CB1R were measured along the membrane using ImageJ, and the distribution of the separation distances between D2 and CB1R was determined[47,66,73–76]. In the cases in which multiple paths connecting particles gave different inter-distance values, the shortest inter-distance was selected and used for distribution analysis. Given that gold particles with edge-to-edge separation distance ≤50 nm are highly suggestive of physical interactions of two detected proteins (that is, a physical coupling complex[47,66,73–76]), distribution analysis of the inter-distance between particles was based on bins of 50 nm.

For all microscopy data, normality tests and statistical analyses were performed using GraphPad Prism software version 7.0a. Information on antibodies used for EM are reported in Supplementary Table 7 (refs. [77–82]).

In vivo single-unit recordings

C57BL/6J WT male mice, injected 2–3 weeks before with ssAAV-9/2-hGFAP-hM3D(Gq)_mCherry-WPRE-hGHp(A) or AAV5. GfaABC1D.cyto-tdTomato.SV40, were anesthetized using chloral hydrate (400 mg kg^{-1} i.p.), supplemented as required to maintain optimal anesthesia throughout the experiment, and placed in the stereotaxic apparatus (Kopf). Their body temperature was maintained at 36 ± 1 °C using a feedback-controlled heating pad. For the placement of a recording electrode, the scalp was retracted, and one burr hole was drilled above the parabrachial pigmented nuclei of the posterior VTA (AP: −3.0 to −3.5 mm from bregma; L: 0.4–0.6 mm from midline; V: 4–5 mm from the cortical surface) according to the Paxinos and Franklin atlas (2004). Extracellular identification of putative DA neurons was based on their location as well as on the set of electrophysiological features that characterize these cells in vivo: (1) a typical triphasic action potential with a marked negative deflection; (2) an action potential width from start to end >2.5 ms; and (3) a slow firing rate (<10 Hz). VTA putative DA neurons were selected only when all the already published criteria were fulfilled[83–86]. Single-unit activity of putative DA neurons was recorded extracellularly using glass micropipettes filled with 2% Chicago sky blue dissolved in 0.5 M sodium acetate (impedance 3–7 MΩ). An injection pipette (20–40 μm in diameter attached 100–150 μm above the recording tip) was used for simultaneous microinjections of CNO (1 mM). This approach allowed us to specifically activate VTA astrocytes in proximity of the glass pipette tip and evaluate their action on the local VTA circuitry. Signal was pre-amplified, amplified (NeuroLog System, Digitimer), filtered (band-pass 500–5,000 Hz)

and displayed on a digital storage oscilloscope. Experiments were sampled on-line and off-line by a computer connected to CED Power 1401 laboratory interface (Cambridge Electronic Design) running the Spike2 software (Cambridge Electronic Design). Single units were isolated, and the spontaneous activity was recorded for a minimum of 3 minutes before local application of CNO (1 mM). A total volume of 30–100 nl was infused using brief (10–100-ms) pressure pulses (40 psi, Picospritzer). One injection maximum per hemisphere was given. For statistical analysis, we calculated the mean firing rate (number of spikes per second) and the percentage of spikes in burst (SiB) before and after CNO application (in 2-minute bins or in the 10 minutes of recording after CNO application). Bursts were defined as the occurrence of two spikes at an inter-spike interval of <80 ms and terminated when the inter-spike interval exceeded 160 ms[87]. At the end of the experiment, negative DC (15 mA for 5 minutes) was passed through the recording electrode to eject Pontamine sky blue, which allowed the anatomical location of the recorded neuron. Mice were then euthanized, and brains were rapidly removed and fixed in 4% paraformaldehyde solution. The position of the electrodes was identified with a microscope in coronal sections (100 μm). Only recordings in the correct area were considered for analysis.

Behavioral test

Viral Injection. C57BL/6J mice were naive and 2 months old at the time of surgery. All mice were anesthetized with a mix of isoflurane/oxygen 2%/1% by inhalation and mounted into a stereotaxic frame (Kopf). Brain coordinates of viral injections in the VTA were chosen in accordance with the *Mouse Brain Atlas*: AP: −3 mm; ML: ± 0.50 mm; DV: −4.7 mm. The volume of AAV injection (AAV9-GFAP-hM3D(Gq)-mCherry or AAV8-GFAP-GFP) was 100 nl per hemisphere. We infused virus through a glass micropipette connected to a 10-μl Hamilton syringe. After infusion, the pipette was kept in place for 6 minutes and then slowly withdrawn.

Locomotor activity. Mice were tested during the first 2 hours of the dark phase in an experimental apparatus consisting of four gray, opaque, open-field boxes (40 × 40 × 40 cm) evenly illuminated by overhead lighting (5 ± 1 lux). Each session was video recorded with ANY-maze tracking software (Stoelting) for 1 hour. In the first day of locomotor activity, all animals received an injection of CNO (3 mg kg^{-1}) 30 minutes before the beginning of the test; 48 hours later, the animals were tested for a second time in the same apparatus with a saline injection.

Drugs

Picrotoxin 50 μM (Sigma-Aldrich); AM251 2-4 μM (Abcam); eticlopride hydrochloride 1 μM (Abcam); SCH-23390 hydrochloride 10 μM (Abcam); D-AP5 50 μM (Abcam); LY-367385 100 μM[88–90] (Abcam); CNO 10 μM (MedChemExpress) and L-741,626 10 μM (Tocris) were bath-applied. L-NAME 100 μM[91–93] (Sigma-Aldrich) and BAPTA 50 mM (Thermo Fisher Scientific) were included in the patch pipette. SKF 38393 1 mM (Abcam) and ATP 4 mM (Sigma-Aldrich) were locally delivered by using a pressure ejection unit.

Data collection and data analysis

Data collection was performed with Clampex 10.5, ANY-maze tracking software, Spike2 software, Leica Application Suite software 2.5.2 and SciScan 1.2. Data analysis was performed with Clampfit 10.5, Origin 8.0 (MicroCal Software), Microsoft Excel 2010, ImageJ 1.49, Sigma Plot 11, ANY-maze tracking software, GraphPad Prism 7.0a, MATLAB R2019b and AQuA 2020.

Statistical analysis

No statistical methods were used to pre-determine sample size, but our sample sizes are similar to those reported in previous publications[19,94–97]. Mice were randomized to groups. Data were not subject to exclusion except in cases of viral vector misplacement. For electrophysiological

experiments in slices, recordings were not considered when the change of series and input resistances were above 20%. In EM, immunohistochemical, single-unit recordings in vivo and behavioral experiments, data collection and analysis were blinded to investigators. Experiments in brain slices were not blinded to investigators. However, the paired design of the study, with comparisons to internal control values in all experiments, and the absence of manual scoring during analysis avoid the experimenter bias. Data are expressed as mean ± s.e.m., except for Fig. 2e. In Fig. 2e, data are presented as a box and whisker plot. Each box is defined by the 25th and 75th percentiles; the central line indicates the median; and the dot indicates the mean value. The whiskers represent the minimum and maximum values in 1.5× the interquartile range. Normality test (Shapiro–Wilk test) was applied to the data before running statistical tests. Based on the normality test result, data before and after burst firing were analyzed using either parametric tests (paired *t*-test and one-sample *t*-test) or non-parametric tests (Wilcoxon signed-rank test and one-sample Wilcoxon signed-rank test) as appropriate. When indicated, data in the absence and presence of antagonist were compared (unpaired *t*-test or Mann–Whitney rank-sum test, depending on the data distribution). The area (μm^2), amplitude (ΔF/F$_0$) and duration (seconds, from 10% onset time to 10% offset time) of Ca^{2+} events extracted by AQuA at basal conditions and after the burst firing were compared using the Kolmogorov–Smirnov test. For EM data analysis, the Mann–Whitney test and contingency Fisher's test were used. For in vivo single-unit recordings and behavioral tests, two-way repeated-measures ANOVA and Bonferroni`s multiple comparison test with adjustment was used. Two-tailed tests were always performed. Statistical differences were established with $P < 0.05$ (*), $P < 0.01$ (**), $P < 0.001$ (***) and $P < 0.0001$ (****).

Reporting summary

Further information on research design is available in the Nature Research Reporting Summary linked to this article.

Data availability

The data that support the findings of this study are available from the corresponding author upon reasonable request. Source data are provided with this paper.

References

53. Li, X., Zima, A. V., Sheikh, F., Blatter, L. A. & Chen, J. Endothelin-1-induced arrhythmogenic Ca^{2+} signaling is abolished in atrial myocytes of inositol-1,4,5-trisphosphate(IP3)-receptor type 2-deficient mice. *Circ. Res.* **96**, 1274–1281 (2005).
54. Marsicano, G. et al. The endogenous cannabinoid system controls extinction of aversive memories. *Nature* **418**, 530–534 (2002).
55. Bello, E. P. et al. Cocaine supersensitivity and enhanced motivation for reward in mice lacking dopamine D2 autoreceptors. *Nat. Neurosci.* **14**, 1033–1038 (2011).
56. Dugué, G. P., Dumoulin, A., Triller, A. & Dieudonné, S. Target-dependent use of coreleased inhibitory transmitters at central synapses. *J. Neurosci.* **25**, 6490–6498 (2005).
57. Bellone, C., Mameli, M. & Lüscher, C. In utero exposure to cocaine delays postnatal synaptic maturation of glutamatergic transmission in the VTA. *Nat. Neurosci.* **14**, 1439–1446 (2011).
58. Chieng, B., Azriel, Y., Mohammadi, S. & Christie, M. J. Distinct cellular properties of identified dopaminergic and GABAergic neurons in the mouse ventral tegmental area. *J. Physiol.* **589**, 3775–3787 (2011).
59. Halassa, M. M., Fellin, T., Takano, H., Dong, J. H. & Haydon, P. G. Synaptic islands defined by the territory of a single astrocyte. *J. Neurosci.* **27**, 6473–6477 (2007).
60. Faber, D. S. & Korn, H. Applicability of the coefficient of variation method for analyzing synaptic plasticity. *Biophys. J.* **60**, 1288–1294 (1991).

61. Wang, Y. et al. Accurate quantification of astrocyte and neurotransmitter fluorescence dynamics for single-cell and population-level physiology. *Nat. Neurosci.* **22**, 1936–1944 (2019).

62. Haustein, M. D. et al. Conditions and constraints for astrocyte calcium signaling in the hippocampal mossy fiber pathway. *Neuron* **82**, 413–429 (2014).

63. Melone, M., Bellesi, M. & Conti, F. Synaptic localization of GLT-1a in the rat somatic sensory cortex. *Glia* **57**, 108–117 (2009).

64. Murphy, M. J. M. & Deutch, A. Y. Organization of afferents to the orbitofrontal cortex in the rat. *J. Comp. Neurol.* **526**, 1498–1526 (2018).

65. Phend, K. D., Rustioni, A. & Weinberg, R. J. An osmium-free method of epon embedment that preserves both ultrastructure and antigenicity for post-embedding immunocytochemistry. *J. Histochem. Cytochem.* **43**, 283–292 (1995).

66. Melone, M., Ciriachi, C., Pietrobon, D. & Conti, F. Heterogeneity of astrocytic and neuronal GLT-1 at cortical excitatory synapses, as revealed by its colocalization with Na^+/K^+-ATPase α isoforms. *Cereb. Cortex* **29**, 3331–3350 (2019).

67. Peters, A., Palay, S. L. & Webster, H. D. The fine structure of the nervous system: the neurons and supporting cells. *Ann. Neurol.* **4**, 588 (1978).

68. DeFelipe, J. Estimation of the number of synapses in the cerebral cortex: methodological considerations. *Cereb. Cortex* **9**, 722–732 (1999).

69. Hervé, D., Pickel, V. M., Joh, T. H. & Beaudet, A. Serotonin axon terminals in the ventral tegmental area of the rat: fine structure and synaptic input to dopaminergic neurons. *Brain Res.* **435**, 71–83 (1987).

70. Tamiya, R., Hanada, M., Kawai, Y., Inagaki, S. & Takagi, H. Substance P afferents have synaptic contacts with dopaminergic neurons in the ventral tegmental area of the rat. *Neurosci. Lett.* **110**, 11–15 (1990).

71. Tagliaferro, P. & Morales, M. Synapses between corticotropin-releasing factor-containing axon terminals and dopaminergic neurons in the ventral tegmental area are predominantly glutamatergic. *J. Comp. Neurol.* **506**, 616–626 (2008).

72. Racz, B. & Weinberg, R. J. The subcellular organization of cortactin in hippocampus. *J. Neurosci.* **24**, 10310–10317 (2004).

73. Petrescu, A. D. et al. Physical and functional interaction of Acyl-CoA-binding protein with hepatocyte nuclear factor-4α. *J. Biol. Chem.* **278**, 51813–51824 (2003).

74. Storey, S. M. et al. Loss of intracellular lipid binding proteins differentially impacts saturated fatty acid uptake and nuclear targeting in mouse hepatocytes. *Am. J. Physiol. Gastrointest. Liver Physiol.* **303**, G837–G850 (2012).

75. Laffray, S. et al. Impairment of GABAB receptor dimer by endogenous 14-3-3ζ in chronic pain conditions. *EMBO J.* **31**, 3239–3251 (2012).

76. Amiry-Moghaddam, M. & Ottersen, O. P. Immunogold cytochemistry in neuroscience. *Nat. Neurosci.* **16**, 798–804 (2013).

77. Ohtani, Y. et al. The synaptic targeting of mGluR1 by its carboxyl-terminal domain is crucial for cerebellar function. *J. Neurosci.* **34**, 2702–2712 (2014).

78. Garcia-Ovejero, D., Arevalo-Martin, A., Paniagua-Torija, B., Sierra-Palomares, Y. & Molina-Holgado, E. A cell population that strongly expresses the CB1 cannabinoid receptor in the ependyma of the rat spinal cord. *J. Comp. Neurol.* **521**, 233–251 (2013).

79. Stojanovic, T. et al. Validation of dopamine receptor DRD1 and DRD2 antibodies using receptor deficient mice. *Amino Acids* **49**, 1101–1109 (2017).

80. Solís, O., Garcia-Montes, J. R., González-Granillo, A., Xu, M. & Moratalla, R. Dopamine D3 receptor modulates l-DOPA-induced dyskinesia by targeting D1 receptor-mediated striatal signaling. *Cereb. Cortex* **27**, 435–446 (2017).

81. Castro-Hernández, J. et al. Prolonged treatment with pramipexole promotes physical interaction of striatal dopamine D3 autoreceptors with dopamine transporters to reduce dopamine uptake. *Neurobiol. Dis.* **74**, 325–335 (2015).

82. Barili, P., Bronzetti, E., Ricci, A., Zaccheo, D. & Amenta, F. Microanatomical localization of dopamine receptor protein immunoreactivity in the rat cerebellar cortex. *Brain Res.* **854**, 130–138 (2000).

83. Grace, A. A. & Bunney, B. S. Intracellular and extracellular electrophysiology of nigral dopaminergic neurons—1. Identification and characterization. *Neuroscience* **10**, 301–315 (1983).

84. Ungless, M. A., Magill, P. J. & Bolam, J. P. Uniform Inhibition of dopamine neurons in the ventral tegmental area by aversive stimuli. *Science* **303**, 2040–2042 (2004).

85. Ungless, M. A. & Grace, A. A. Are you or aren't you? Challenges associated with physiologically identifying dopamine neurons. *Trends Neurosci.* **35**, 422–430 (2012).

86. Lecca, S., Melis, M., Luchicchi, A., Muntoni, A. L. & Pistis, M. Inhibitory inputs from rostromedial tegmental neurons regulate spontaneous activity of midbrain dopamine cells and their responses to drugs of abuse. *Neuropsychopharmacology* **37**, 1164–1176 (2012).

87. Grace, A. A. & Bunney, B. S. The control of firing pattern in nigral dopamine neurons: burst firing. *J. Neurosci.* **4**, 2877–2890 (1984).

88. Mannaioni, G., Marino, M. J., Valenti, O., Traynelis, S. F. & Conn, P. J. Metabotropic glutamate receptors 1 and 5 differentially regulate CA1 pyramidal cell function. *J. Neurosci.* **21**, 5925–5934 (2001).

89. Bridi, M. et al. Transcriptional corepressor SIN3A regulates hippocampal synaptic plasticity via Homer1/mGluR5 signaling. *JCI Insight* **5**, e92385 (2020).

90. Salah, A. & Perkins, K. L. Effects of subtype-selective group I mGluR antagonists on synchronous activity induced by 4-aminopyridine/CGP 55845 in adult guinea pig hippocampal slices. *Neuropharmacology* **55**, 47–54 (2008).

91. Pfeiffer, S., Leopold, E., Schmidt, K., Brunner, F. & Mayer, B. Inhibition of nitric oxide synthesis by N^G-nitro-L-arginine methyl ester (L-NAME): requirement for bioactivation to the free acid, N^G-nitro-L-arginine. *Br. J. Pharmacol.* **118**, 1433–1440 (1996).

92. Lu, Q. et al. Nitric oxide induces hypoxia ischemic injury in the neonatal brain via the disruption of neuronal iron metabolism. *Redox Biol.* **6**, 112–121 (2015).

93. Ivanova, V. O., Balaban, P. M. & Bal, N. V. Nitric oxide regulates GluA2-lacking AMPAR contribution to synaptic transmission of CA1 apical but not basal dendrites. *Front. Synaptic Neurosci.* **13**, 1–12 (2021).

94. Congiu, M., Trusel, M., Pistis, M., Mameli, M. & Lecca, S. Opposite responses to aversive stimuli in lateral habenula neurons. *Eur. J. Neurosci.* **50**, 2921–2930 (2019).

95. Sagheddu, C. et al. Inhibition of N-acylethanolamine acid amidase reduces nicotine-induced dopamine activation and reward. *Neuropharmacology* **144**, 327–336 (2019).

96. Poyraz, F. C. et al. Decreasing striatopallidal pathway function enhances motivation by energizing the initiation of goal-directed action. *J. Neurosci.* **36**, 5988–6001 (2016).

97. Boekhoudt, L. et al. Enhancing excitability of dopamine neurons promotes motivational behaviour through increased action initiation. *Eur. Neuropsychopharmacol.* **28**, 171–184 (2018).

Acknowledgements

Author contributions

Competing interests

Additional information
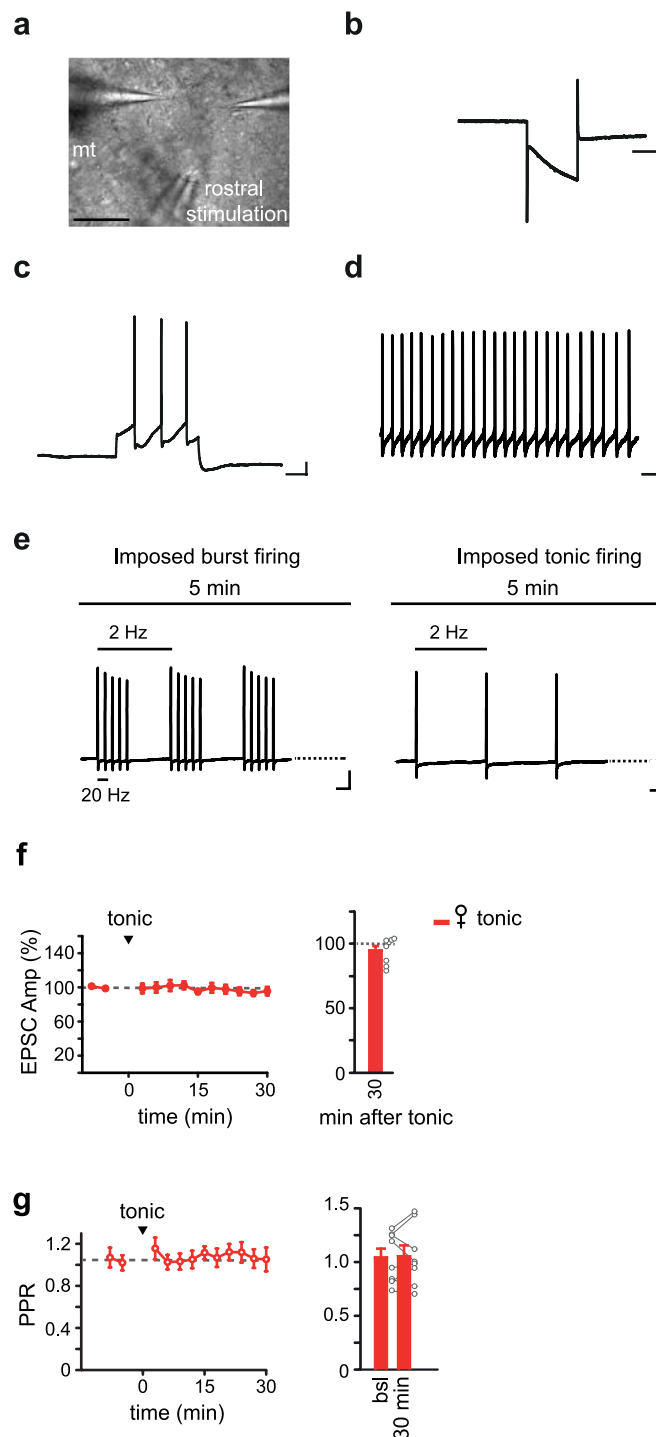
Extended Data Fig. 1 | Electrophysiological properties of DA neurons recorded from VTA slice preparations. a) Differential interference contrast image of the lateral VTA showing the recording pipettes on a pair of DA neurons and the theta-capillary for extracellular stimulation of rostral glutamatergic afferents (mt, medial terminal nucleus of the accessory optical tract). Scale bar, 100 μm. **b)** Representative large Ih current elicited by a hyperpolarizing step. Scale bars, 200 pA, 500 ms. **c)** Representative slow depolarizing potential preceding the action potential during a depolarizing current step injection. Scale bars, 10 mV, 200 ms. **d)** Representative spontaneous low-frequency tonic firing. Scale bars, 20 mV, 2 s. **e)** Representative burst and tonic firing evoked by current step injections. Scale bars, 20 mV, 100 ms. **f)** EPSC amplitude after tonic firing protocol in wt female mice (n = 8 from 5 mice, p = 0.169, two-tailed paired t-test). **g)** Time course of paired-pulse ratio (PPR) values in female mice (n = 8), before and after tonic firing protocol (arrowhead). Right, mean PPR values before and 30 min after tonic firing (p = 0.827, two-tailed paired t-test). Data are represented as mean ± SEM.

a

b

c
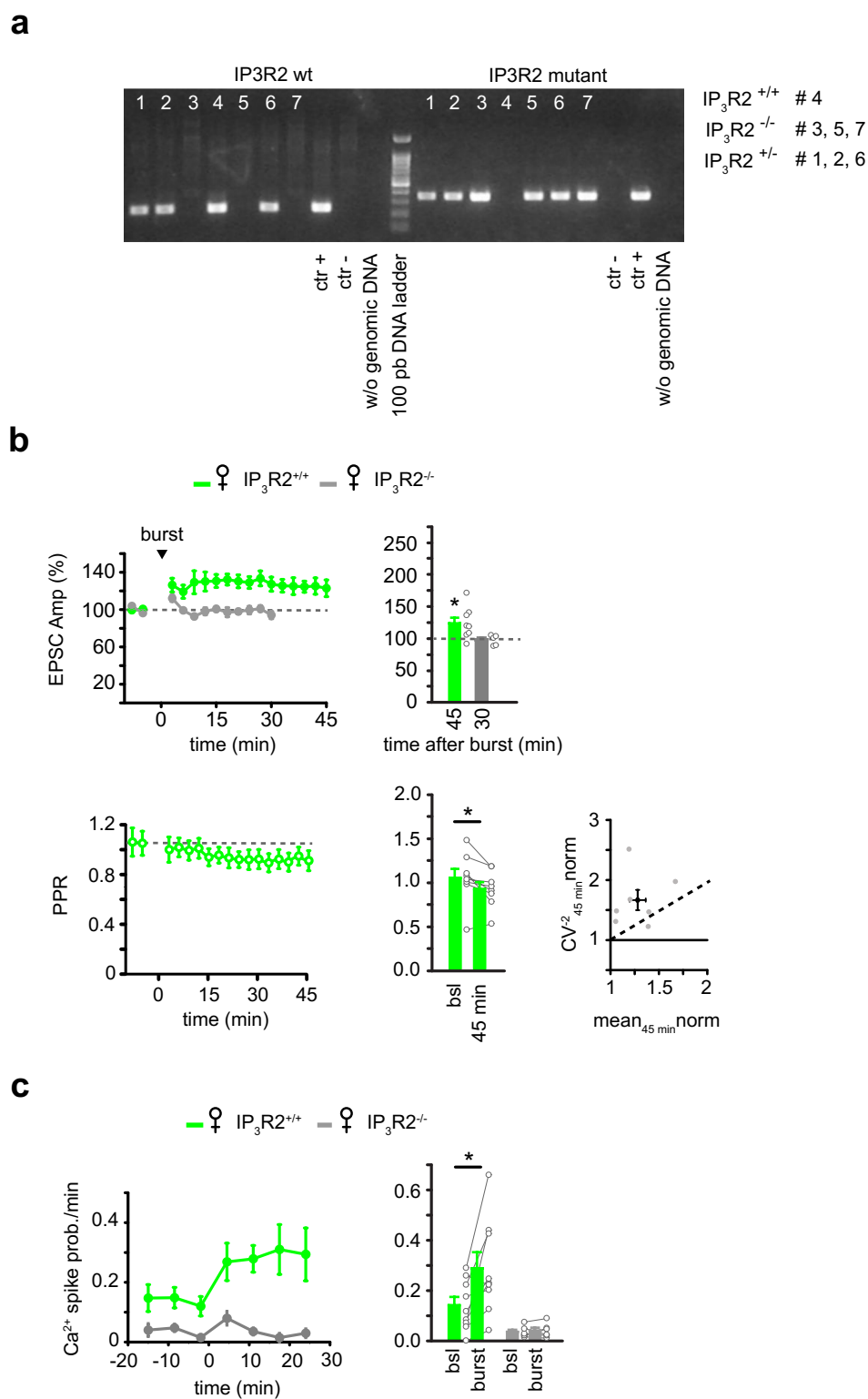
Extended Data Fig. 2 | bLTP can be evoked in IP₃R2$^{+/+}$ but not in IP₃R2$^{-/-}$ young female littermates. a) Example of mouse genotyping by PCR amplification of the IP₃R2 wt (~200 bp) and mutant (~400 bp) alleles from genomic DNA. **b)** Top, bLTP can be evoked in IP₃R2$^{+/+}$ (n = 8 from 8 mice, p = 0.029, two-tailed One Sample t-test), but not in IP₃R2$^{-/-}$ (n = 5 from 4 mice, p = 0.524, two-tailed One Sample t-test) young female littermates. Bottom, the bLTP in IP₃R2$^{+/+}$ female mice is accompanied by a reduced PPR (p = 0.031, two-tailed paired t-test), similarly to that observed in C57BL/6J young female mice (see Fig. 1). Analysis of the coefficient of variation of EPSCs, 45 min after burst firing for potentiated cells in IP₃R2$^{+/+}$ young mice (black circle, mean value). **c)** DA neuron bursts evoke an increase of the Ca²⁺ spike probability/min in astrocytes from IP₃R2$^{+/+}$ (n = 9 from 5 mice, p = 0.017, two-tailed paired t-test), but not in astrocytes from IP₃R2$^{-/-}$ (n = 6 from 4 mice, p = 0.533, two-tailed paired t-test) young female littermates. Data are represented as mean ± SEM.
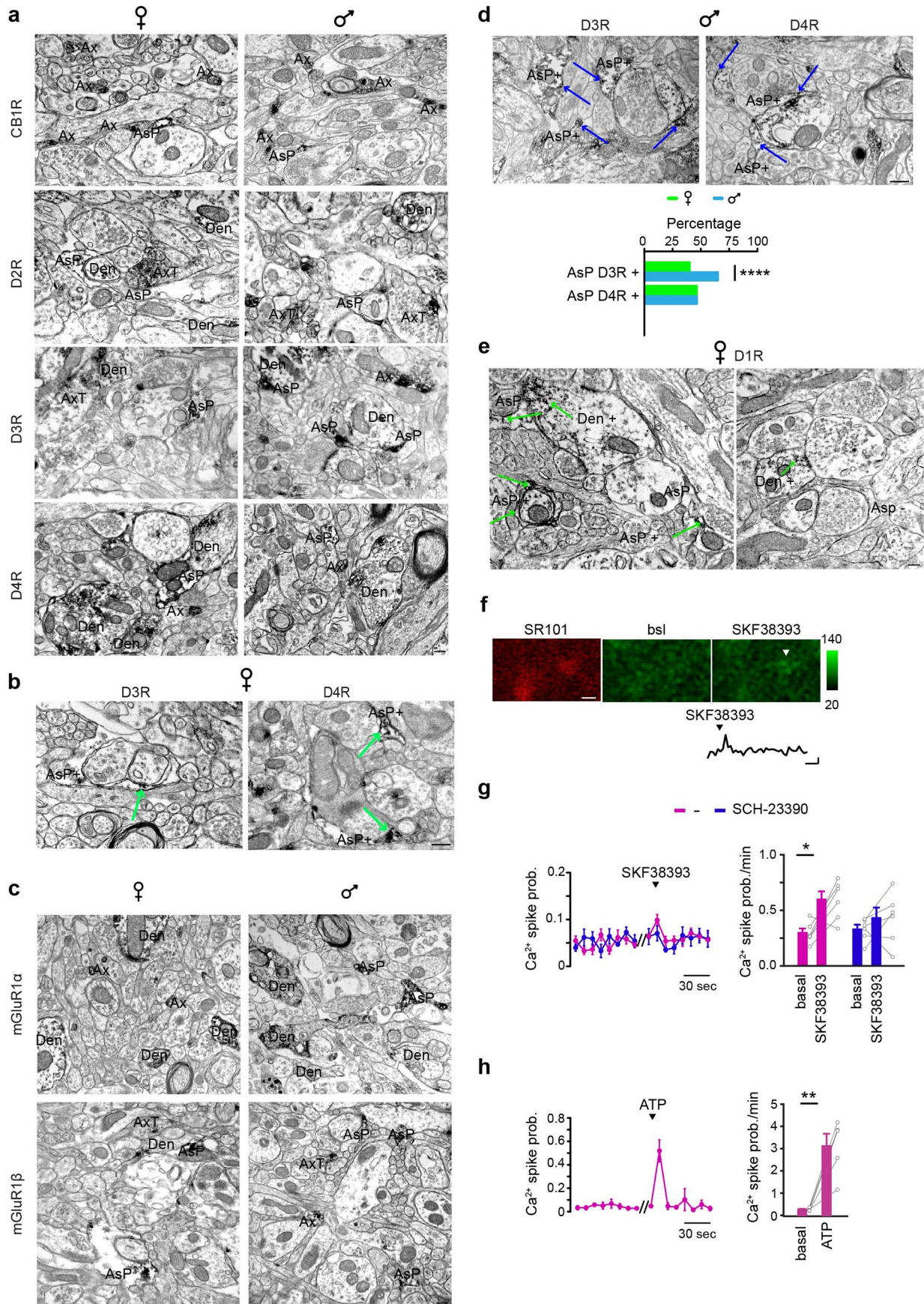
Extended Data Fig. 3 | See next page for caption.

Extended Data Fig. 3 | Expression of CB1, D2, D3, D4, D1, mGluR1α and mGluR1β receptors in neuronal and astrocytic compartments in the VTA of P16 female and male mice. a) EM image showing CB1, D2, D3 and D4R immunoreactivity at neuronal compartments (Den, dendrites; Ax, axons; AxT, axon terminals) and astrocytic processes (AsP), in the lateral VTA of P16 female and male mice. Quantitative analysis of the distribution of immunoreactive profiles in female and male mice is reported in Supplementary Table 1. Scale bar, 250 nm. **b)** Representative pre-embedding EM images showing the expression of D3 and D4Rs at astrocytic processes (AsP) from the lateral VTA of a P16 female mouse. Green arrows indicate the presence of immunopositive products in AsP (AsP+). Scale bar, 300 nm. **c)** EM images of mGlu1α and mGlu1βR-immunoreactivity in the lateral VTA of P16 female and male mice. mGluR1α is largely detectable in dendrites (Den), in some astrocytic processes (AsP) and axons (Ax; see Supplementary Table 3 for quantitative distribution of mGluR1α immunoreactivity in both female and male). The mGluR1β is detectable in AsP, AxT (including those making an asymmetric synaptic contact) and Den (see Supplementary Table 3 for quantitative distribution of mGluR1β immunoreactivity in both female and male). Scale bar, 250 nm. **d)** Upper panel, the same as in (b), but in the lateral VTA of a P16 male mouse. Lower panel, quantification and comparison (two sided contingency Fisher's test) of D3 ($p < 0.0001$) and D4R ($p > 0.999$) expression in female and male young mice. **e)**

Representative ultrastructural fields of D1 immunoreactivity in the neuropil of lateral VTA in P16 female mice. Examples of neuronal (Den, dendrites) and astroglial (AsP, astrocytic processes) D1 immunoreactivity are illustrated. Quantitative analysis of the distribution of immunoreactive profiles is reported in Supplementary Table 4. Scale bar: 250 nm. **f)** Upper panel, representative fluorescence images showing two SR-101-positive astrocytes and the Ca^{2+} increase evoked in one of them (arrowhead, detected with Fluo-4), after locally applying the D1-type R agonist SKF 38393 (1 mM in glass pipette). Scale bar, 5 μm. Lower panel, time course of the Ca^{2+} transient shown on the left. Scale bars, 10 s, 10 %. **g)** Left, time course of the mean Ca^{2+} spike probability, in 10 sec bins, at basal conditions and after SKF 38393 challenge, both in the absence and presence of the D1-type R antagonist SCH-23390 (10 μM). Right, bar chart of the mean Ca^{2+} spike probability/min before and immediately after SKF 38393 challenge to show the Ca^{2+} response of VTA astrocytes to SKF 38393 (without SCH-23390, n = 6 from 4 mice, p = 0.022; with SCH-23390, n = 6 from 4 mice, p = 0.325; two-tailed paired t-test). **h)** Same as in g), but after ATP (4 mM in glass pipette) in five of the six slices previously challenged with SKF 38393 (n = 5 from 3 mice, p = 0.007, two-tailed paired t-test). Note that, compared to the strong astrocyte response to ATP, VTA astrocytes show a small, but significant Ca^{2+} response to D1-type receptor activation that is abolished in the presence of the D1-type receptor antagonist SCH-23390. Data are represented as mean ± SEM.

a

AAV-GFAP-mCherry-hM3D

b
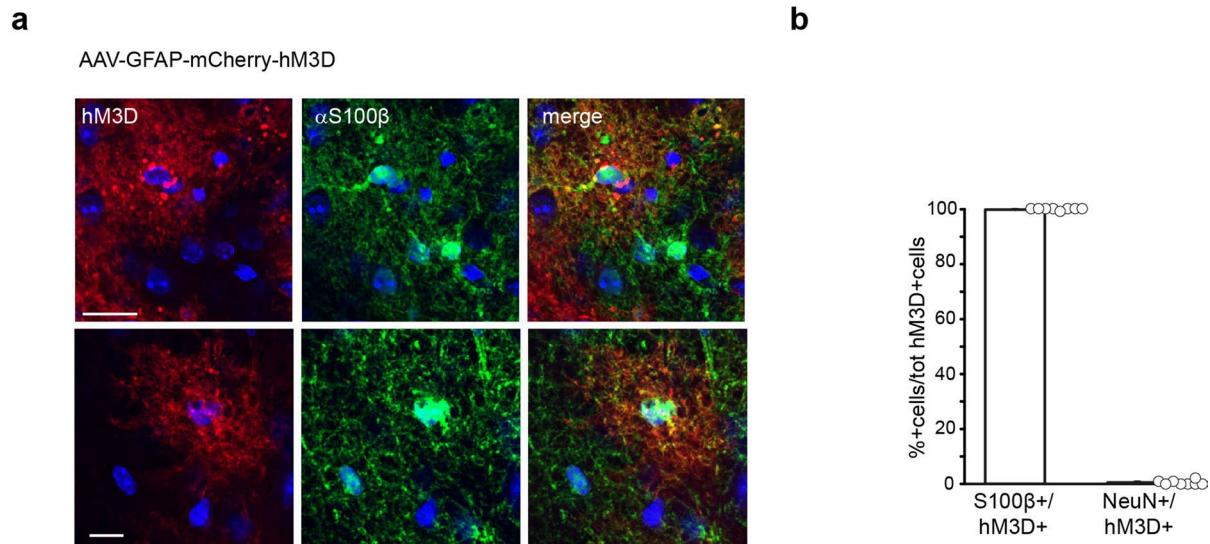

Extended Data Fig. 4 | Targeted expression of mCherry-hM3D in VTA astrocytes from young male mice. a) High magnification fluorescence images of the VTA from a mouse injected with AAV-9/2-hGFAP-hM3D(Gq)_mCherry-WPRE-hGHp(A), showing colocalization in astrocyte processes of mCherry-hM3D and the astrocyte marker S100β. Scale bar, upper panel 20 μm, lower panel 10 μm. **b)** Bar chart showing the percentage of mCherry positive cells that are astrocytes (S100β positive) or neurons (NeuN positive). αS100β; n = 1106 mCherry-hM3D+ cells from 4 mice, 8 slices; αNeuN, n = 1039 mCherry-hM3D+ cells from 4 mice, 8 slices. Data are represented as mean ± SEM.
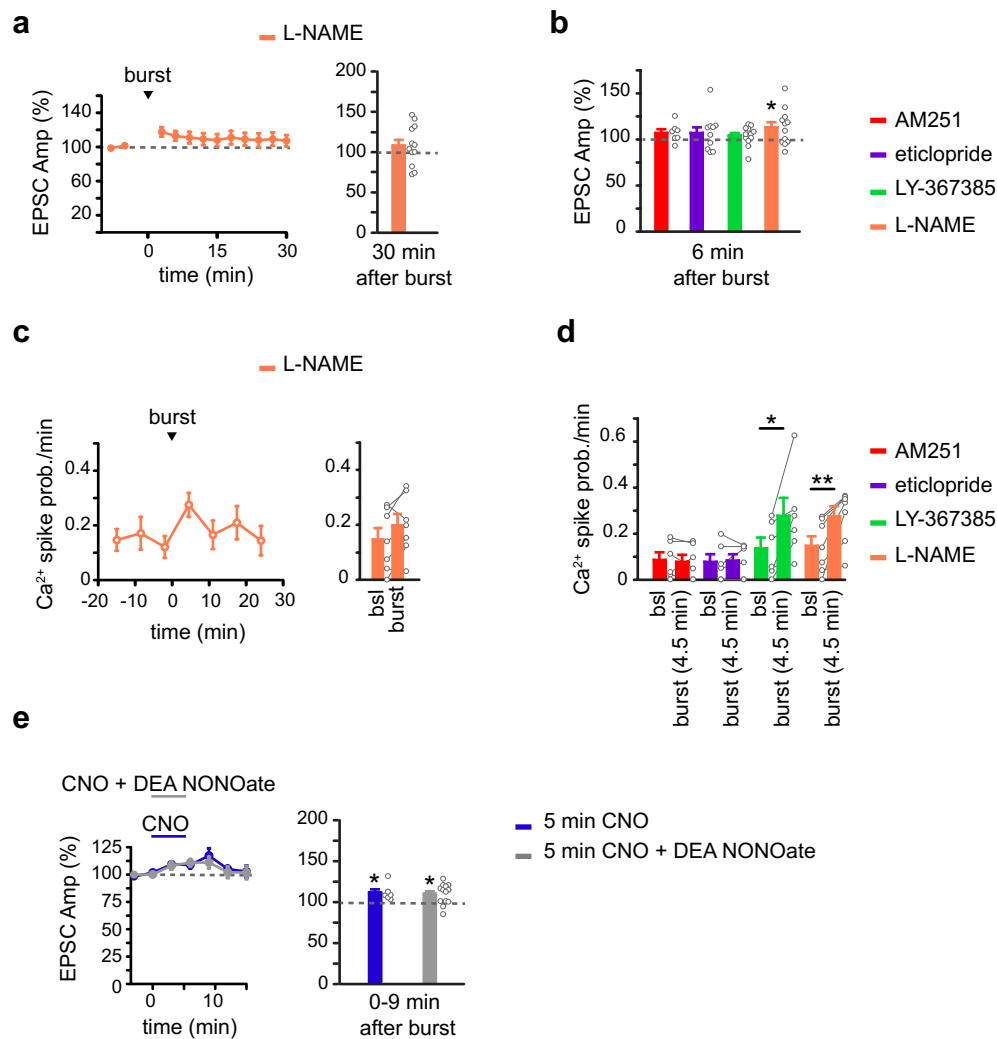
Extended Data Fig. 5 | Effects of the NO synthase inhibitor L-NAME on bLTP and astrocyte Ca^{2+} response to DA neuron burst firing. a) Time course and bar chart of EPSC amplitude in the presence of the NO synthase inhibitor L-NAME (100 µM in the patch pipette of the burst firing DA neuron, n = 12 from 9 mice, p = 0.277; two-tailed One sample t-test). **b)** Mean amplitude of normalized EPSCs in female mice, 6 min after bursts, in the presence of different antagonists (AM251, n = 7 from 4 mice, p = 0.105; eticlopride, n = 10 from 8 mice, p = 0.291; LY-367385, n = 12 from 9 mice, p = 0.215; L-NAME, n = 12, from 9 mice p = 0.044; two-tailed One sample t-test). **c)** Time course and bar chart of astrocytic Ca^{2+} spike probability/min in the presence of L-NAME before and after burst firing (100 µM, n = 7 from 4 mice, p = 0.075; two-tailed paired t-test). **d)** Mean astrocytic Ca^{2+} spike probability/min in female mice, at basal conditions and 4.5 min after burst, in the presence of different antagonists (AM251, n = 6 from 3 mice, p = 0.671; eticlopride, n = 6 from 3 mice, p = 0.673; LY-367385, n = 6 from 4 mice, p = 0.048; L-NAME, n = 7 from 4 mice, p = 0.009; two-tailed paired t-test). **e)** A 5 min bath perfusion of CNO (10 µM), in the absence and presence of DEA NONOate (10 µM), transiently (in the first 9 min) increases EPSC amplitude of DA neurons in male mice expressing hM3D in astrocytes (CNO, n = 7 from 6 mice, p = 0.016, two-tailed One sample Wilcoxon Signed Rank test; CNO + DEA NONOate, n = 13 from 9 mice, p = 0.013, two-tailed One sample t-test). These experiments were performed in the presence of AM251 and eticlopride. Data are represented as mean ± SEM.
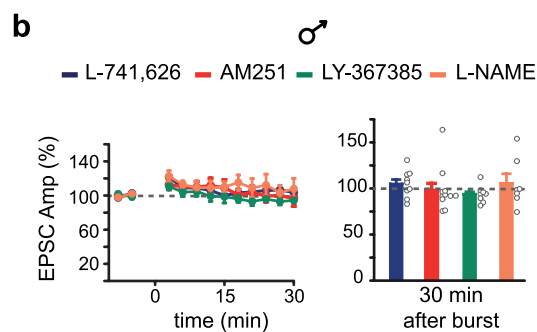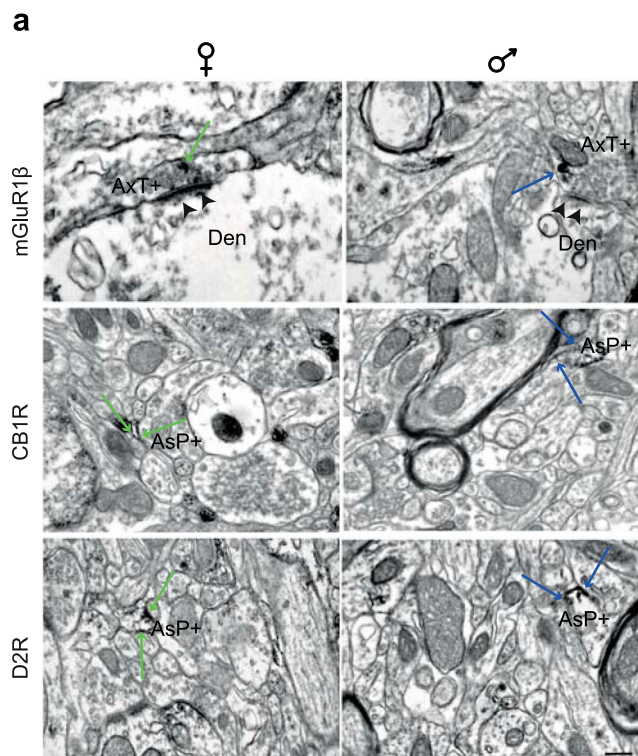
Extended Data Fig. 6 | The mechanism of bLTP generation in young female mice is preserved in adult mice. a) Representative EM images of mGluR1β expression at axon terminals (AxT+) forming asymmetric synaptic contacts (arrowheads) with dendrites (Den) and CB1 and D2R localization at astrocytic processes (AsP+) from adult female and male mice. Green and blue arrows indicate the presence of immunopositive products in female and male, respectively. Scale bar, 300 nm. **b)** Time course and bar chart of the mean amplitude of normalized EPSCs in adult male mice in the presence of different antagonists (L-741,626 (D2R) 10 μM, n = 9 from 7 mice, p = 0.34, two-tailed One Sample t-test; AM251 (CB1R), n = 11 from 8 mice, p = 0.24, two-tailed One Sample Wilcoxon signed Rank test; LY-367385 (mGluR1), n = 8 from 7 mice, p = 0.096, two-tailed One Sample t-test; L-NAME (NO synthase), n = 7 from 5 mice, p = 0.604, two-tailed One Sample t-test). As in young mice, bLTP generation in adult mice requires eCB-DA signaling and mGluR activation. Data are represented as mean ± SEM.

a

AAV-GFAP-mCherry-CRE

b

c

AAV-GFAP-GCamp6

d

e

AAV-GFAP-mCherry-hPMCA2w/b

f
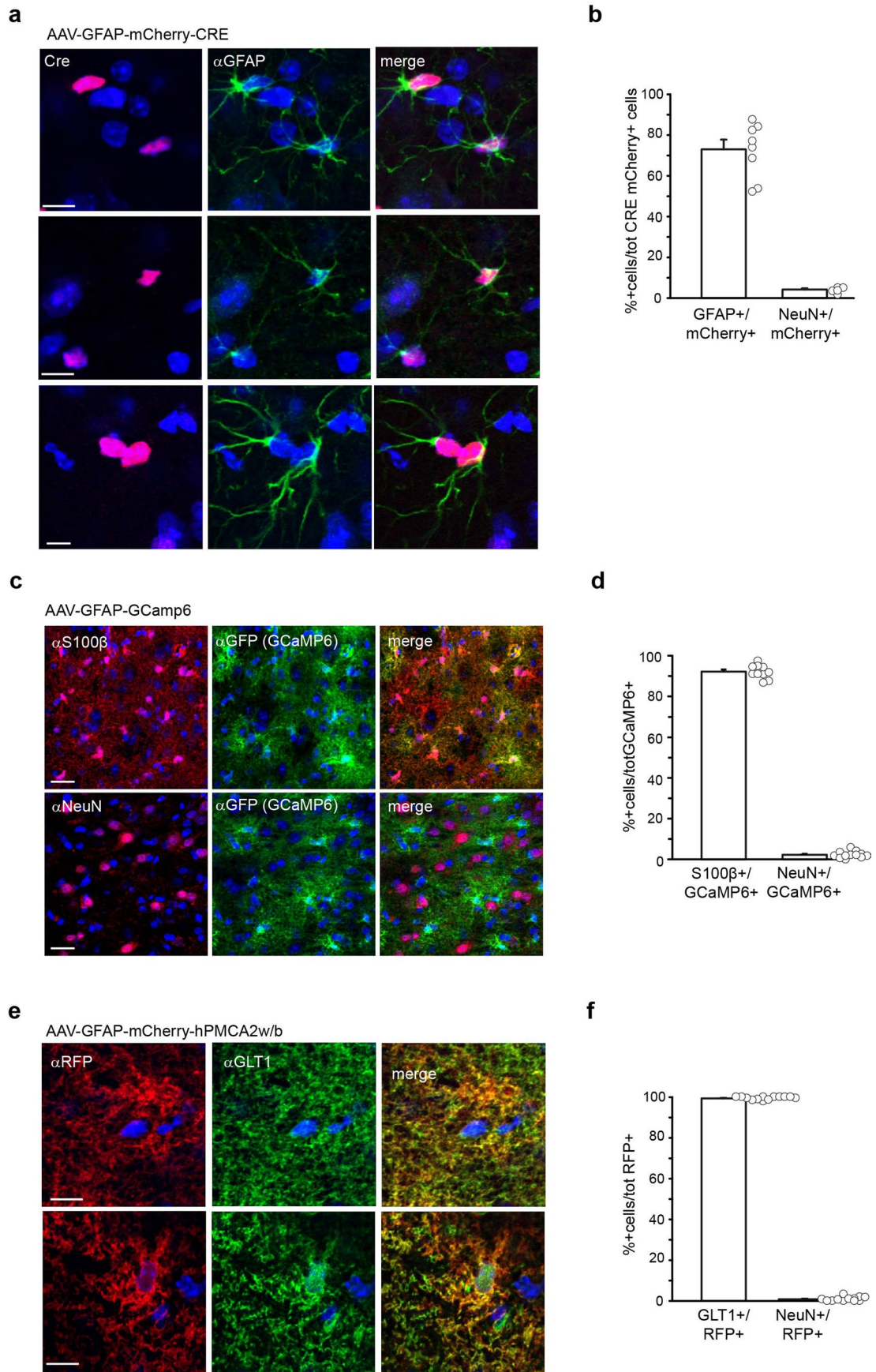
Extended Data Fig. 7 | See next page for caption.

Extended Data Fig. 7 | Targeted expression of mCherry-Cre, GCaMP6f and mCherry-hPMCA2w/b in VTA astrocytes from adult mice. a) High magnification fluorescence images of the VTA from an adult male mouse injected with AAV9-hGFAP-mCherry_iCre-WPRE-hGHp(A), illustrating the nuclear localization of mCherry-Cre in GFAP-positive astrocytes. Scale bar, 10 µm. **b)** Bar chart showing the percentage of nuclear mCherry-Cre positive cells that are astrocytes (GFAP positive) or neurons (NeuN positive). αGFAP; n = 1265 mCherry-Cre+ cells from three mice, 8 slices; αNeuN, n = 747 mCherry-Cre+ cells from three mice, 5 slices. **c)** Confocal microscope fluorescence images of the VTA from an adult male mouse injected with AAV5.GfaABC1D.cytoGCaMP6f.SV40, showing the green fluorescence of GCaMP6f (α-GFP), nuclear Top-Ro3 (blue) and the specific red staining for either neurons (α-NeuN) or astrocytes (α-S100β). Merged images, localization of GCaMP6f in astrocytes (S100β-positive cells)

and not in neurons (NeuN-positive cells). Scale bar, 25 µm. **d)** Bar chart showing the percentage of GCaMP6f positive cells that are astrocytes (S100β positive) or neurons (NeuN positive). αS100β; n = 1383 GCaMP6f+ cells from four mice, 10 slices; αNeuN, n = 1586 GCaMP6f+ cells from four mice, 12 slices. **e)** High magnification fluorescence images of the VTA from an IP$_3$R2$^{-/-}$ adult mouse injected with AAV5-GfaABC1D-mCherry-hPMCA2w/b.SV40, showing the expression of the Ca^{2+} pump hPMCA2w/b (α-RFP red staining) in GLT1-positive astrocytic processes. Scale bar, 10 µm. **f)** Bar chart showing the percentage of cells expressing the Ca^{2+} pump hPMCA2w/b that are astrocytes (GLT-1 positive) or neurons (NeuN positive). αGLT1; n = 2164 mCherry-hPMCA2w/b(αRFP)+ cells from four mice, 13 slices; αNeuN, n = 1902 mCherry-hPMCA2w/b(αRFP)+ cells from four mice, 12 slices. Data are represented as mean ± SEM.

a

b
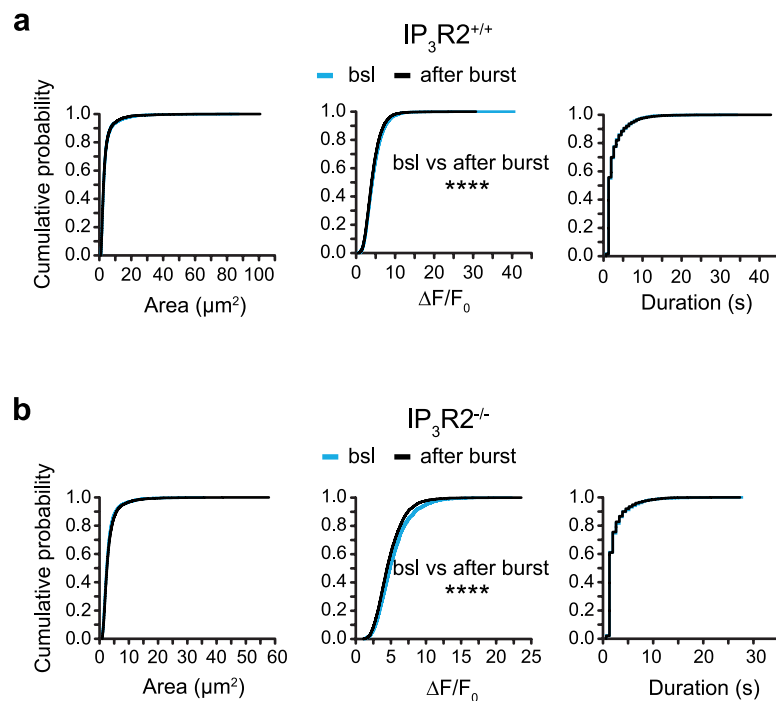
Extended Data Fig. 8 | Area, amplitude and duration of Ca²⁺ events extracted by AQuA before and after DA neuron burst. a) Cumulative distributions of the area (μm^2), amplitude ($\Delta F/F0$) and duration (s) of Ca²⁺ events extracted by AQuA, before and after DA neuron burst in $IP_3R2^{+/+}$ mice (before burst, 6942 events; after burst, 10760 events; area, $p = 0.218$; amplitude, $p < 0.0001$; duration, $p = 0.968$; two-tailed Kolmogorov-Smirnov test). **b)** Same as in a), but from $IP_3R2^{-/-}$ mice (before burst, 2483 events; after burst, 4483 events; area, $p = 0.083$; $\Delta F/F0$, $p < 0.0001$; duration, $p = 0.967$; two-tailed Kolmogorov-Smirnov test).
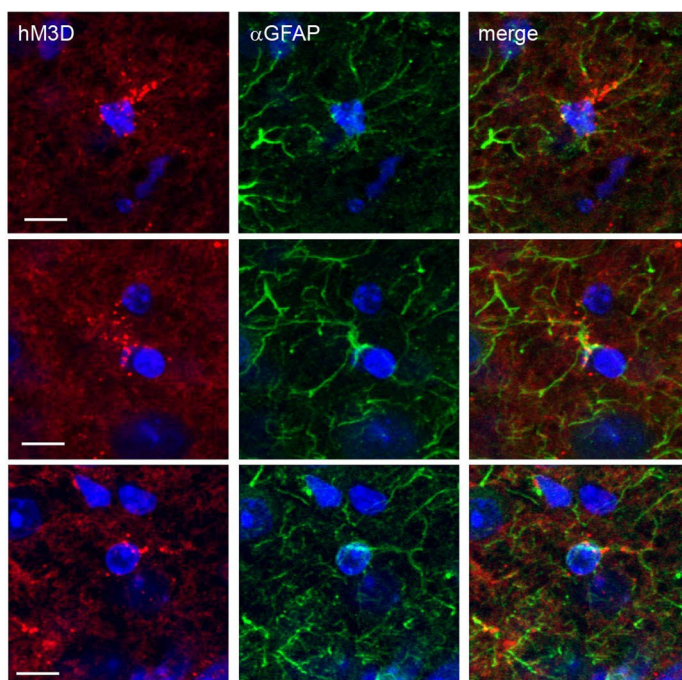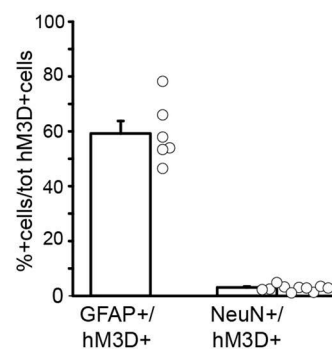
a

AAV-GFAP-mCherry-hM3D
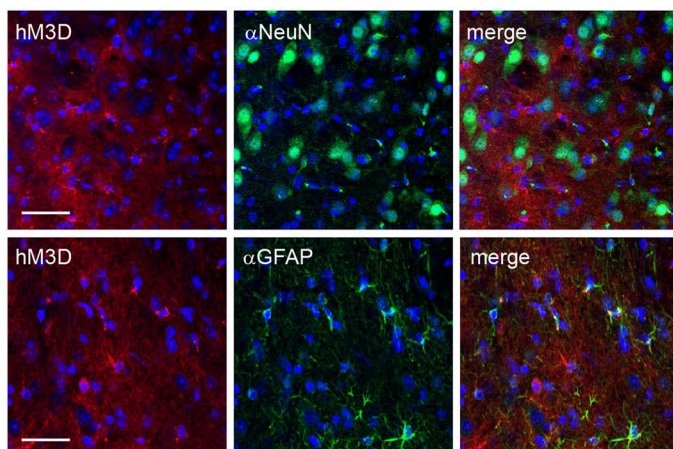
b

AAV-GFAP-mCherry-hM3D

c


Extended Data Fig. 9 | Targeted expression of mCherry-hM3D in VTA astrocytes from adult male mice. a) Confocal microscope fluorescence images of the VTA from an adult mouse injected with AAV-9/2-hGFAP-hM3D(Gq)_mCherry-WPRE-hGHp(A), showing the red fluorescence of mCherry-hM3D (red), nuclear Top-Ro3 (blue) and the specific green staining for either neurons (α-NeuN) or astrocytes (α-GFAP). Merged images, localization of hM3D in astrocytes (GFAP-positive cells) and not in neurons (NeuN-positive cells). Scale bars, 50 µm. **b)** High magnifications of the VTA from a mouse injected with AAV-9/2-hGFAP-hM3D(Gq)_mCherry-WPRE-hGHp(A), illustrating the colocalization of mCherry-hM3D with the astrocyte marker GFAP in astrocyte processes. Scale bars, 10 µm. **c)** Bar chart showing the percentage of mCherry-hM3D positive cells that are astrocytes (GFAP positive) or neurons (NeuN positive). αGFAP; n = 683 mCherry-hM3D+ cells from 3 mice, 6 slices; αNeuN, n = 1127 mCherry-hM3D+ cells from five mice, 10 slices. Data are represented as mean ± SEM.

a

b

c

d
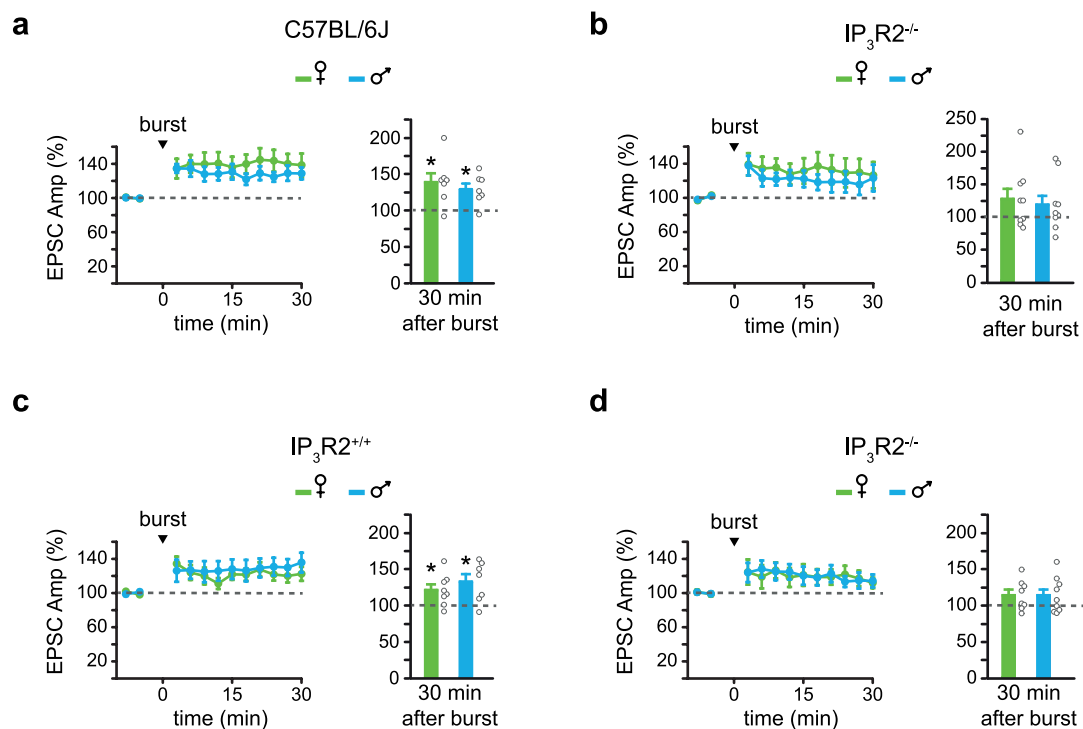
Extended Data Fig. 10 | DA neuron burst firing modulation of excitatory synapses onto adjacent DA neurons in adult IP$_3$R2$^{+/+}$ and IP$_3$R2$^{-/-}$ littermates and non-littermates female and male mice. a, b) Time course and bar chart of the mean amplitude of normalized EPSCs in adult female and male C57BL/6J (a) and IP$_3$R2$^{-/-}$ (b) non littermates mice (C57BL/6J; female mice, n = 7 from 6 mice, p = 0.019; male mice, n = 7 from 5 mice, p = 0.01; IP$_3$R2$^{-/-}$; female mice, n = 9 from 7 mice, p = 0.108; male mice, n = 9 from 9 mice, p = 0.194; two-tailed One sample t-test). **c, d)** Same as in a, b) but from adult female and male IP$_3$R2$^{+/+}$ (c) and IP$_3$R2$^{-/-}$ (d) littermate mice (IP$_3$R2$^{+/+}$; female mice, n = 8 from 7 mice, p = 0.028; male mice, n = 7 from 5 mice, p = 0.021; IP$_3$R2$^{-/-}$; female mice, n = 8 from 7 mice, p = 0.087; male mice, n = 9 from 7 mice, p = 0.112; two-tailed One sample t-test). Data are represented as mean ± SEM.

nature research

Corresponding author(s): GOMEZ-GONZALO MARTA, CARMIGNOTO GIORGIO

Last updated by author(s): Sep 19, 2022

Reporting Summary

Nature Research wishes to improve the reproducibility of the work that we publish. This form provides structure for consistency and transparency in reporting. For further information on Nature Research policies, see our Editorial Policies and the Editorial Policy Checklist.

Statistics

For all statistical analyses, confirm that the following items are present in the figure legend, table legend, main text, or Methods section.

n/a	Confirmed	
☐	☒	The exact sample size (n) for each experimental group/condition, given as a discrete number and unit of measurement
☐	☒	A statement on whether measurements were taken from distinct samples or whether the same sample was measured repeatedly
☐	☒	The statistical test(s) used AND whether they are one- or two-sided *Only common tests should be described solely by name; describe more complex techniques in the Methods section.*
☐	☒	A description of all covariates tested
☐	☒	A description of any assumptions or corrections, such as tests of normality and adjustment for multiple comparisons
☐	☒	A full description of the statistical parameters including central tendency (e.g. means) or other basic estimates (e.g. regression coefficient) AND variation (e.g. standard deviation) or associated estimates of uncertainty (e.g. confidence intervals)
☐	☒	For null hypothesis testing, the test statistic (e.g. F, t, r) with confidence intervals, effect sizes, degrees of freedom and P value noted *Give P values as exact values whenever suitable.*
☒	☐	For Bayesian analysis, information on the choice of priors and Markov chain Monte Carlo settings
☒	☐	For hierarchical and complex designs, identification of the appropriate level for tests and full reporting of outcomes
☒	☐	Estimates of effect sizes (e.g. Cohen's d, Pearson's r), indicating how they were calculated

Our web collection on statistics for biologists contains articles on many of the points above.

Software and code

Policy information about availability of computer code

Data collection	Clampex 10.5, ANY-maze tracking software, Spike2 software, Leica Application Suite (LAS) sofware 2.5.2, SciScan 1.2
Data analysis	Clampfit 10.5, Origin 8.0, Microsoft Excel 2010, ImageJ 1.49, SigmaPlot 11, ANY-maze tracking software, GraphPad Prism Software v.7.0a, AQuA 2020, MATLAB R2019b

For manuscripts utilizing custom algorithms or software that are central to the research but not yet described in published literature, software must be made available to editors and reviewers. We strongly encourage code deposition in a community repository (e.g. GitHub). See the Nature Research guidelines for submitting code & software for further information.

Data

Policy information about availability of data

All manuscripts must include a data availability statement. This statement should provide the following information, where applicable:
- Accession codes, unique identifiers, or web links for publicly available datasets
- A list of figures that have associated raw data
- A description of any restrictions on data availability

The data that support the findings of this study are available from the corresponding author upon reasonable request.

Field-specific reporting

Please select the one below that is the best fit for your research. If you are not sure, read the appropriate sections before making your selection.

☒ Life sciences ☐ Behavioural & social sciences ☐ Ecological, evolutionary & environmental sciences

For a reference copy of the document with all sections, see nature.com/documents/nr-reporting-summary-flat.pdf

Life sciences study design

All studies must disclose on these points even when the disclosure is negative.

Sample size	No statistical methods were used to predetermine sample size but our sample sizes are similar to those reported in previous publications (Gomez-Gonzalo et al, 2019; Congiu et al, 2019; Sagheddu et al, 2019; Poyraz et al, 2016; Boekhoudt et al, 2018).
Data exclusions	Data were not subject to exclusion except in cases of viral vector misplacement. For electrophysiological experiments in slices, recordings were not considered when the change of series and input resistances were above 20%.
Replication	To obtain reproducible findings all experiments were repeated, as indicated in text and/or figure legends.
Randomization	Allocation was random.
Blinding	In electron microscopy, inmunohistochemical, single unit recordings in vivo and behaviour experiments, data collection and analysis were blinded to investigators. Experiments in brain slices were not blinded to investigators. However, the paired design of the study, with comparisons to internal control values in all experiments, and the absence of manual scoring during analysis avoid the experimenter bias.

Reporting for specific materials, systems and methods

We require information from authors about some types of materials, experimental systems and methods used in many studies. Here, indicate whether each material, system or method listed is relevant to your study. If you are not sure if a list item applies to your research, read the appropriate section before selecting a response.

Materials & experimental systems

n/a	Involved in the study
☐	☒ Antibodies
☒	☐ Eukaryotic cell lines
☒	☐ Palaeontology and archaeology
☐	☒ Animals and other organisms
☒	☐ Human research participants
☒	☐ Clinical data
☒	☐ Dual use research of concern

Methods

n/a	Involved in the study
☒	☐ ChIP-seq
☒	☐ Flow cytometry
☒	☐ MRI-based neuroimaging

Antibodies

Antibodies used	anti-NeuN (RRID:AB_2298772, 1:200 mouse, Thermofisher_Millipore, Lot n° 3061189, MAB377), anti-glial fibrillary acidic protein (GFAP, RRID:AB_10013382, 1:400 rabbit, Dako Agilent, Lot n° 00005193, Z0334), anti-S100B (RRID:AB_2315306, 1:400 rabbit, Dako Agilent, Z031129), anti-glutamate transporter 1 (GLT1, RRID:AB_90949, 1:400 guinea pig, Abcam, Lot n° 3135983, AB1783), secondary antibodies conjugated with AlexaFluor-488 (1:500; Lot n°1741782, A21202, RRID: AB_141607, donkey anti-mouse; Lot n° 2289872, A21206, RRID: AB-2535792, donkey anti-rabbit; Lot n° 982288, A11073, RRID: AB_2534117, goat anti-guinea pig, Invitrogen Thermo-Scientific). anti-RFP (RRID:AB_2209751, 1:1000 rabbit, Rockland , Lot n° 42872, 600-401-379), anti-mouse (or anti-guinea pig) AlexaFluor-488 conjugated together the anti-rabbit AlexaFluor-555 conjugated (A21430 donkey anti-rabbit, Invitrogen Thermo-Scientific, 1:500), anti-S100B (RRID:AB_2620025, 1:300 quinea pig, Synaptic System, Lot n° 1-9, 287004), antibodies plus donkey immunoglobulins anti-mouse Alexa 556 conjugated (RRID:AB_2534012, 1:500, Thermofisher, Lot n° 2160040, A10036) or goat anti-guinea pig Alexa 546 conjugated (RRID:AB_2534118, 1:500, Thermofisher, Lot n° 1073002, A11074), Alexa 488 conjugated rabbit polyclonal anti-GFP (Thermofisher, Lot n° 2406568, A21311, RRID:AB_221477 1:250), Top-Ro3 (Invitrogen Thermo-Scientific, 1:1000), tyrosine-hydroxylase (primary antibodies from Millipore, AB1542, RRID:AB_90755 64 ; 1:500), anti-mGLUR1a (Frontier Institute, Rb-Af811, RRID:AB_2571799, lot n° not provided by the manufacturer, rabbit, 1:200), anti-mGLUR1b (Frontier Institute, Rb-Af250, lot n° not provided by the manufacturer, RRID: AB_2616586, rabbit, 1:100), anti-CB1 (Frontier Institute, GP-Af530, lot n° not provided by the manufacturer, RRID: AB_2571593, Guinea pig, 1:200 IP, 1:25 IG), anti-D1 (Sigma-Aldrich, ABD2944, lot n° 113713, RRID: AB_1840787, rat, 1:80 IP), anti-D2 (Millipore, AB5084P, lot n° 3041811 and lot n° 3590058, RRID:AB_2094980, rabbit, 1:100 IP, 1:10 IG), anti-D3 (Alomone, ADR-003, lot n° ADR003AN0250 and lot n° ADR003AN0350, RRID:AB_2039830, rabbit, 1:100), anti-D4 (Millipore, AB324405, lot n° 2817178, RRID:AB_564550, rabbit, 1:1000), anti-rabbit Biotinylated (Jackson, 711-066-152, lot n° 122168, RRID:AB_2340594, 1:500), anti- guinea pig Biotinylated (Jackson, 706-066-148, lot n° 117526, RRID:AB_2340452, 1:500), anti-guinea pig 18nm gold (Jackson, 706-215-148, lot n° 79414, AB_2340466; 1:20), anti-rat Biotinylated (Vector, BA-4001, lot n° Y0908, RRID:AB_10015300, 1:200), anti-rabbit 12nm gold (Jackson, 711-205-152, lot n° 121086, RRID:AB_2340610, 1:20).

| Validation | In the methods section validation with knockout mice or preadsorption of immunogen peptide has been indicated for antibodies used in electron microcopy. For immunihistochemical stainings commercial, broadly used antibodies have been employed. |

Animals and other organisms

Policy information about studies involving animals; ARRIVE guidelines recommended for reporting animal research

| Laboratory animals | C57BL/6J, IP3R2KO (Li et al, 2005), Drd2-floxed (Bello et al, 2011), Cnr1-floxed (Marsicano et al, 2002) female and/or male mice at P14-17 and P30-70 were used. Mice were housed under a 12-h light–dark cycle (7.00 to 19.00 light), with a room temperature of 22°C and humidity of 60%. |

| Wild animals | No wild animals were used in this study. |

| Field-collected samples | No field collected samples we used in this study. |

| Ethics oversight | Animal care, handling and procedures were carried out in accordance with National (D.L. n.26, March 14, 2014) and European Community Council (2010/63/UE) laws, policies, and guidelines, and were approved by the Italian Ministry of Health (D2784.N.TU2/2018; 40A31.N.ZUK, 754/2018-PR, 749/2017-PR and 639/2020-PR) and by the local Institutional Animal Care and Use Committee of the Università di Padova, Università Politecnica delle Marche and IIT. |

Note that full information on the approval of the study protocol must also be provided in the manuscript.